

AGN Triality of Triple Mergers: Detection of Faint X-ray Point Sources

ADI FOORD,^{1,2} KAYHAN GÜLTEKIN,¹ JESSIE C. RUNNOE,³ AND MICHAEL J. KOSS⁴

¹*Department of Astronomy and Astrophysics, University of Michigan, Ann Arbor, MI 48109*

²*Kavli Institute of Particle Astrophysics and Cosmology, Stanford University, Stanford, CA 94305*

³*Department of Physics and Astronomy, Vanderbilt University, Nashville, TN 37235*

⁴*Eureka Scientific Inc, Oakland, CA, 94602*

ABSTRACT

We present results from our X-ray analysis of the first systematic search for triple AGN in nearby ($z < 0.077$) triple galaxy mergers. We analyze archival *Chandra* observations of 7 triple galaxy mergers with BAYMAX (Bayesian Analysis of Multiple AGN in X-rays), fitting each observation with single, dual, and triple X-ray point source models. In doing so, we conclude that 1 triple merger has one X-ray point source (SDSS J0858+1822, although it’s unlikely to be an AGN); 5 triple mergers are likely composed of two X-ray point sources (NGC 3341, SDSS J1027+1749, SDSS J1631+2352, SDSS J1708+2153, and SDSS J2356–1016); and one system is composed of three X-ray point sources (SDSS J0849+1114). By fitting the individual X-ray spectra of each point source, we analyze the 2–7 keV luminosities as well as the levels of obscuration associated with each potential AGN. We find that 4/5 dual X-ray point source systems have primary and secondary point sources with bright X-ray luminosities ($L_{2-7\text{keV}} > 10^{40}\text{erg s}^{-1}$), possibly associated with 4 new undetected dual AGN. The dual and triple point source systems are found to have physical separations between 3–9 kpc and flux ratios between 2×10^{-3} –0.84. A multi-wavelength analysis to determine the origin of the X-ray point sources discovered in this work is presented in our companion paper (Foord et al. 2020c).

Keywords: galaxies: active — galaxies — X-rays — galaxies: interactions

1. INTRODUCTION

Systems with multiple supermassive black holes (SMBHs) are expected as a result of hierarchical galaxy formation (e.g., White & Rees 1978). If two massive galaxies are in the process of merging, it is expected that dynamical friction will drag their respective nuclear SMBHs toward the center of the gravitational potential well (see, e.g., Begelman et al. 1980). Through the process of merging, significant quantities of gas can be efficiently funneled down to physical scales at which the SMBHs can accrete – and the multiple SMBH systems can become multiple active galactic nuclei (AGN; Barnes & Hernquist 1991; Di Matteo et al. 2008; Anglés-Alcázar et al. 2017). Thus pairs of AGN, such as dual AGN (two AGN that are in the process of merging, but are not yet gravitationally bound) and binary AGN (two interacting AGN that are gravitationally bound), are signposts of ongoing galaxy formation, and represent unique systems where the link between environment and black hole growth (or, lack thereof) can be probed.

An important subset of the multiple SMBH population are triple SMBHs, and in particular, *nearby* triple SMBH systems. Nearby triple SMBHs ($z < 0.3$) are

theorized to play important roles in the coalescence of SMBHs and the stochastic gravitational wave background (GWB). For example, without additional interactions from a tertiary SMBH, two interacting SMBHs may not merge within the Hubble time due to an empty loss cone (Milosavljević & Merritt 2003), producing a stochastic GWB undetectable by pulsar timing arrays (PTAs; “the nightmare scenario”, Dvorkin & Barausse 2017). Although triaxial potentials have been shown to prevent SMBH stalling (Vasiliev et al. 2015), it is not clear that triaxiality will sufficiently refill the loss cone in time (Merritt & Valluri 1996). More importantly, the process of two SMBHs becoming bound via dynamical friction may be far slower than initially thought (Tremmel et al. 2015), and it has recently been found that gas dynamics may cause the pair of SMBHs to stall at ~ 1 kpc (Muñoz et al. 2019; Duffell et al. 2019). Interactions with a third SMBH can enhance the loss cone refilling rate by disturbing stellar orbits (Perets & Alexander 2008), shrinking the binary semimajor axis and increasing the eccentricity via the Kozai–Lidov mechanism (Blaes et al. 2002). All these effects can dramatically reduce the merger time of binaries by more than a factor

of 10 (Blaes et al. 2002). On top of this, it is predicted that the SMBH binary population driving the detectable GWB signal comes from redshifts close to $z = 0.3$ (Kelley et al. 2017), and thus the rate of nearby triple AGN has significant implications for the GWB measurable with PTAs. Lastly, triple AGN are expected to be common. A recent study on Illustris SMBH binaries found that $>30\%$ of AGN pairs have subsequent merger events, over a large range of redshift (Kelley et al. 2017), while analysis of the Millennium simulation found that 42% of massive ($10^{11} < M_* < 10^{12}$) galaxies undergo more than one significant merger (Ryu et al. 2018).

A handful of multiple AGN candidates have been identified using multiwavelength diagnostics (Liu et al. 2011a; Schawinski et al. 2012; De Rosa et al. 2015; Kalfountzou et al. 2017); however to date, only one serendipitously discovered X-ray triple AGN has been identified (Pfeifle et al. 2019a). This is may be due to observational constraints and the lack of systematic surveys searching for triple AGN.

Regarding the lack of observational constraints, confirmation of multiple AGN systems requires high spatial resolution X-ray observations. Although other wavelengths and techniques are useful for finding candidate multiple AGN systems, they are not always reliable (Koss et al. 2011). For example, double-peaked optical emission lines are insufficient to confirm dual AGN due to ambiguity in interpretation, as single AGN spectra are known to also have double-peaked characteristics (Comerford et al. 2015; Nevin et al. 2016). On top of this, it is difficult to identify multiple AGN using optical line diagnostics as a result of optical extinction and contamination from star formation (e.g., Koss et al. 2012). This is especially problematic for multiple AGN systems, as late-stage mergers tend to be highly obscured (e.g., Kocevski et al. 2015; Koss et al. 2016; Ricci et al. 2017a; Blecha et al. 2018; De Rosa et al. 2018; Koss et al. 2018; Lanzuisi et al. 2018; Torres-Albà et al. 2018; however see Gross et al. 2019 for results that argue X-ray deficits in merging AGN may be due to heightened star formation rather than elevated X-ray obscuration).

X-rays are thus crucial to detecting closely separated triple AGN. Nuclear point sources with 2–10 keV X-ray luminosities $L_X > 10^{40}$ erg s $^{-1}$ are almost always SMBHs (Foord et al. 2017a; Lehmer et al. 2019), and *Chandra* can uniquely resolve them. Although various X-ray surveys targeting dual AGN exist, all X-ray confirmed dual AGN have large physical separations (> 1 kpc, see Deane et al. 2014; De Rosa et al. 2019; Hou et al. 2020) and count ratios ($f \sim 1$, where f represents the ratio of the X-ray counts associated with the secondary to that of the primary AGN). Specifically, because 1'' cor-

responds to roughly 1 kpc at $z = 0.05$, many *Chandra* investigations are limited to dual AGN with large separations. On top of this, past analyses have been limited to detecting sources with similar brightness. We have developed BAYMAX, a code that quantitatively and rigorously analyzes whether a given *Chandra* source is more likely composed of one or multiple point sources (Foord et al. 2019, 2020). BAYMAX (i) takes calibrated *Chandra* events and compares them to the expected distribution of counts for single/multiple point source models; (ii) calculates a Bayes factor to determine which model is preferred, automatically taking into account model complexity; (iii) calculates likely values for separations (r) and count ratios (f); and (iv) fits spectra to each component. Analyses without BAYMAX are likely to lead to false negatives/positives (e.g., Koss et al. 2015; Foord et al. 2020), especially systems with small separations ($r < 1''$) and fainter secondaries.

Regarding the lack of systematic surveys searching for triple AGN, in this paper we present results from our systematic search for triple AGN in nearby triple galaxy mergers. In the following paper, we analyze a sample of 7 optically-identified, nearby ($z < 0.1$), triple galaxy mergers, that have existing archival *Chandra* data. We analyze the *Chandra* observations using BAYMAX, with the goal of identifying faint multiple point source systems that may otherwise go undetected. The *Chandra* observations of 3 of these triple merger systems were previously analyzed in studies focusing on multiple AGN (Pfeifle et al. 2019a; Bianchi et al. 2013), which we now re-analyze via our robust statistical analysis. The remaining 4 have no existing analyses of their *Chandra* observations.

The remainder of the paper is organized into 5 sections. In section 2 we introduce the sample and the existing multi-wavelength coverage. In section 3 we review the Bayesian framework behind BAYMAX and the models used to fit each observation. In section 4 we present our results from running BAYMAX on the *Chandra* observations and quantify the strength of each result. In section 5 we analyze the X-ray spectra of each multiple AGN candidate in order to measure their 2–keV luminosities and levels of surrounding gas. Lastly, we summarize our findings in section 6. Throughout the paper we assume a Λ CDM universe, where $H_0 = 69.6$, $\Omega_M = 0.286$, and $\Omega_\Lambda = 0.714$.

2. SAMPLE

Our sample was created by cross-matching the AllWISE AGN catalog (Secrest et al. 2015) with the SDSS Data Release 16 (SDSS DR16) catalog (Ahumada et al. 2019), for all AGN within $z < 0.3$. We then visu-

ally identify the systems composed of three interacting galaxies via the SDSS DR16 data, and we further filter the sample by enforcing that (i) a photometric or spectroscopic redshift measurement is available for each galaxy in a triple merger system and (ii) that the respective redshifts of each galaxy in a triple merger system are consistent with one another at the 3σ confidence level. While spectroscopic measurements of the redshift are generally well constrained (with fractional errors on the order of $\sim 10^{-3}$), photometric measurements of the redshift tend to have larger error bars and are estimated by SDSS via the kd-tree nearest neighbor fitting procedure (see Csabai et al. 2007 for explicit details). Because at least one galaxy member in each triple merger has a spectroscopic redshift measurement, we assume this value for all members (see Table 1). From this larger sample of 12 triple galaxy mergers, 4 systems have existing, on-axis, archival *Chandra* observations: SDSS J1708+2153, SDSS J2356–1015, SDSS J1631+2252, SDSS J0849+1114. To this list, we add 3 triple galaxy mergers from the literature with archival *Chandra* and SDSS DR16 observations that meet our redshift criteria as described above: NGC 3341 (Bianchi et al. 2013), SDSS J0858+1822 (Liu et al. 2011b) and SDSS J1027+1749 (Liu et al. 2011a). Thus, while all of our triple mergers have *Chandra* and SDSS DR16 coverage, only 4 are included in the AllWISE AGN catalog. Because we visually identify each triple galaxy merger using the SDSS catalog snapshots, we are most sensitive to triple galaxy mergers with angular separations between galactic nuclei that are larger than the SDSS optical fiber ($\sim 3''$), corresponding to physical separations larger than 3 kpc and smaller than 15 kpc. Given these larger angular separations, the ability for BAYMAX to probe fainter sources is of particular importance to our study. Specifically, in past systematic X-ray studies searching for dual AGN, flux ratios between the primary and secondary AGN are large (~ 1 in Hou et al. 2020); and in the largest X-ray study to date (Koss et al. 2012), the typical flux ratio was approximately 0.08. However, BAYMAX is capable of detecting dual AGN systems down to flux ratios $\lesssim 10^{-2}$.

The *Chandra* observations of 3/7 systems in our sample have been previously analyzed for the presence of multiple AGN: SDSS J0849+1114 (classified as a triple AGN system in Liu et al. 2019; Pfeifle et al. 2019a), NGC 3341 (classified as a single AGN system in Bianchi et al. 2013), and SDSS J2356–1016 (classified as a single AGN system in Pfeifle et al. 2019b). The remaining four systems have no existing analyses on the possible multiplicity of AGN in the *Chandra* observations, al-

though SDSS J1027+1749 was claimed as triple AGN in Liu et al. (2011a) based on optical emission diagnostics. The archival *Chandra* observations for all of these systems were part of different programs studying merging systems: SDSS J0849+1114, SDSS J0858+1822, and SDSS J1027+1749 were observed by *Chandra* as part of a program analyzing triple-AGN candidates; SDSS J1708+2153 and SDSS J1631+2252 were observed as part of a program studying mergers in BAT AGN (e.g. Koss et al. 2010); SDSS J2356–1016 was observed as part of a program studying interacting galaxies with extreme red mid-IR colors; while the *Chandra* observations NGC 3341 was not part of a larger program, but the system was similarly observed to search for the presence of 3 AGN. Analyzing these galaxies using BAYMAX, we aim to identify new X-ray point sources, as well as re-evaluate the true nature of the previously claimed multiple AGN systems. The galaxies are located at redshifts $0.059 < z < 0.077$, and three (SDSS J0849+1114, SDSS J0858+1822, SDSS J1027+1749) have additional multi-band HST/WFC3 (F506W and F5336W) imaging (PI: Liu, Proposal ID: 13112). In Table 1 we list the properties of each triple merger system, while in Table 2 we list the *Chandra* observation information.

2.1. X-ray Data Analysis

Each *Chandra* observation was on-axis and placed on the back-illuminated S3 chip of the ACIS detector. We follow a similar data reduction as described in previous *Chandra* analyses searching for AGN (e.g., Foord et al. 2017a,b, 2019, 2020), using *Chandra* Interactive Analysis of Observations software (CIAO) v4.12 (Fruscione et al. 2006).

We first correct for astrometry, cross-matching the *Chandra*-detected point-like sources with the SDSS Data Release 9 (SDSS DR9) catalog. The *Chandra* sources used for cross-matching are detected by running `wavdetect` on the reprocessed level-2 event file. We require each observation to have a minimum of 3 matches with the SDSS DR9, and each matched pair to be less than $2''$ from one another. Five of the seven systems meet the criterion for astrometrical corrections, while the remaining 2 observations were taken in sub-arrays and do not have enough X-ray point sources to match with the SDSS DR9 catalog. However, we note that the lack of astronomical corrections have no effect on our X-ray data analysis, as the locations of each putative AGN are assumed to be relative to the primary X-ray point source, and our prior distributions for locations of each AGN are wide enough to account for the relative astrometric shifts between the *Chandra* and optical observations (see section 3 for more details). Lastly, for

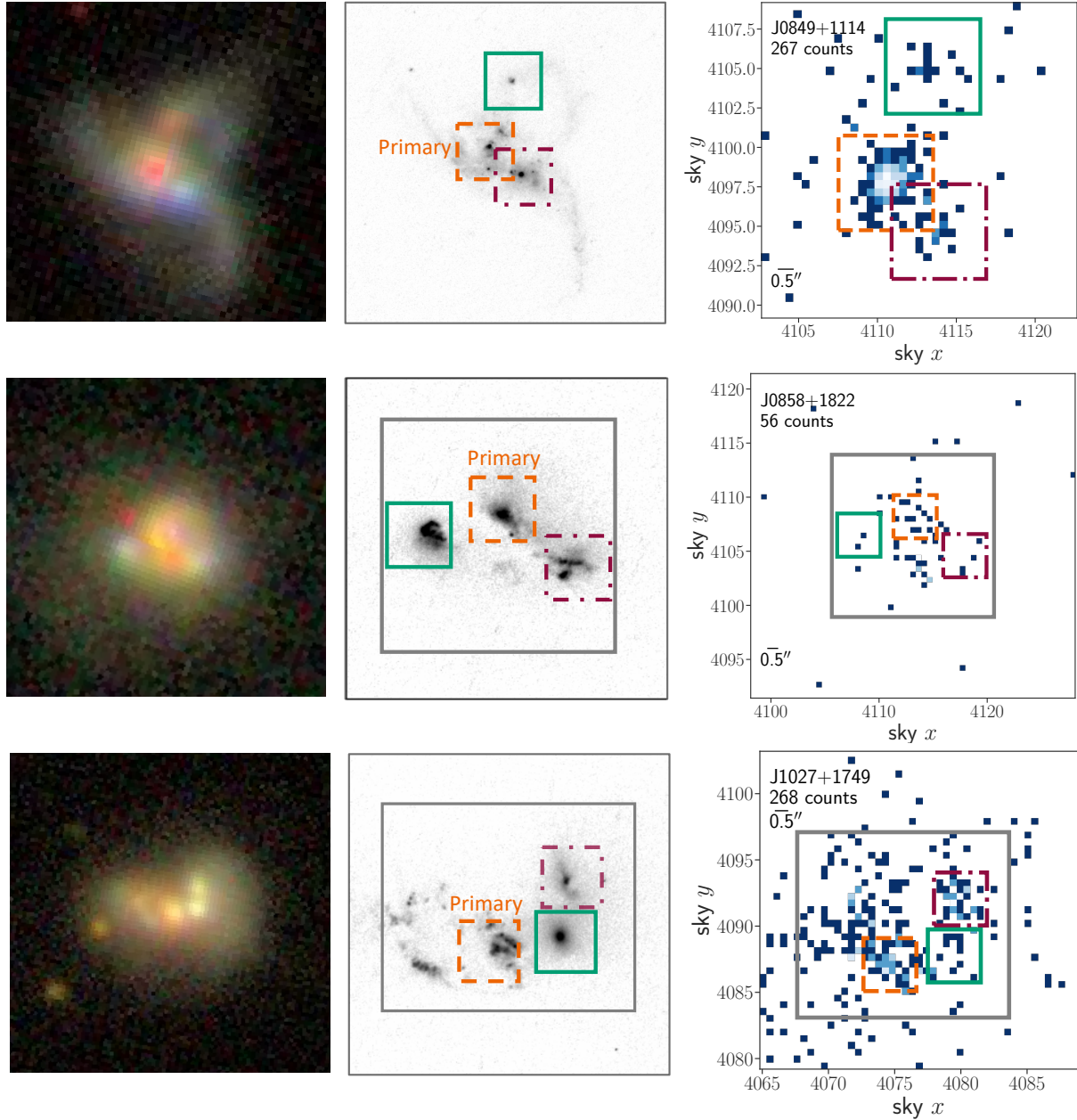


Figure 1. SDSS gri color composite observations (*left*), *HST* F366W observations (*center*), and *Chandra* 0.5–8 keV observations (*right*) of the triple mergers in our sample with *HST* observations. In the *HST* and *Chandra* datasets, we show the sky x , sky y region, within which the informative priors for μ (sky x , y , position) are constrained to in orange (dashed), purple (dot-dashed), and green boxes. When using non-informative priors, the central locations for the primary and secondary are allowed to be anywhere within the FOV shown in the X-ray image. For SDSS J0858+1822 and SDSS J1027+1729 we denote the region within which the diffuse emission background component is restricted to with a gray box. Additionally, for SDSS J0849+1114 we show the combined X-ray emission for all *Chandra* observations, where we use the best-fit astrometric shift values as found by BAYMAX. The X-ray images have been binned to *Chandra*'s native pixel resolution. In all panels, north is up and east is to the left, and a $0''.5$ bar is shown to scale.

Table 1. Triple Galaxy Merger Sample Properties

Galaxy Name (1)	α (2)	δ (3)	Redshift (4)	D_A (Mpc) (5)	$\Delta\theta$ (") (6)	r (kpc) (7)
SDSS J084905.51+111447.2	08:49:05.51	+11:14:47.26	0.077	306.4
SDSS J084905.51+111447.2 SW	08:49:05.41	+11:14:45.94	2.3	3.4
SDSS J084905.51+111447.2 NW	08:49:05.43	+11:14:50.97	3.6	5.3
SDSS J085837.67+182223.3	08:58:37.67	+18:22:23.35	0.059	236.9
SDSS J085837.67+182223.3 SW	08:58:37.52	+18:22:21.56	2.8	3.2
SDSS J085837.67+182223.3 SE	08:58:37.85	+18:22:22.43	2.8	3.2
SDSS J102700.40+174900.8	10:27:00.56	+17:49:00.38	0.066	262.9
SDSS J102700.40+174900.8 N	10:27:00.38	+17:49:02.89	3.6	4.6
SDSS J102700.40+174900.8 W	10:27:00.39	+17:49:00.95	2.4	3.0
NGC 3341	10:42:31.75	+05:02:52.82	0.027	112.6
NGC 3341 SW	10:42:31.47	+05:02:37.80	15.6	8.5
NGC 3341 NW	10:42:32.05	+05:02:41.95	9.6	5.2
SDSS J163115.52+235257.5	16:31:15.52	+23:52:57.51	0.059	236.9
SDSS J163115.52+235257.5 NE	16:31:15.62	+23:52:59.56	2.5	2.9
SDSS J163115.52+235257.5 NW	16:31:15.41	+23:53:08.44	11	12.6
SDSS J170859.12+215308.0	17:08:59.12	+21:53:08.08	0.072	284.8
SDSS J170859.12+215308.0 NE	17:08:59.42	+21:53:13.51	6.6	9.1
SDSS J170859.12+215308.0 SW	17:08:58.40	+21:53:05.12	10.5	14.5
SDSS J235654.30-101605.3	23:56:54.30	-10:16:05.31	0.074	292.0
SDSS J235654.30-101605.3 SE	23:56:54.49	-10:16:07.40	3.5	4.9
SDSS J235654.30-101605.3 NE	23:56:54.78	-10:16:01.06	8.2	11.6

Note. – Columns: (1) Galaxy name; (2) R.A. and (3) Dec. (J2000) from SDSS DR16; (4) spectroscopic redshift from SDSS DR16; (5) angular diameter distance; (6) angular separation from primary galaxy; (7) projected physical separation from primary galaxy.

Table 2. *Chandra* Observation Information

Galaxy Name (1)	<i>Chandra</i> Obs. ID (2)	<i>Chandra</i> Exp. Time (s) (3)
SDSS J084905.51+111447.2	14969	19800
...	18196	20980
SDSS J085837.67+182223.3	14970	19800
SDSS J102700.40+174900.8	14971	49410
NGC 3341	13871	49330
SDSS J163115.52+235257.5	13901	18150
SDSS J170859.12+215308.0	13903	18200
SDSS J235654.30-101605.3	18195	8620

Note. – Columns: (1) Galaxy name; (2) *Chandra* Observation ID; (3) exposure time of *Chandra* observation.

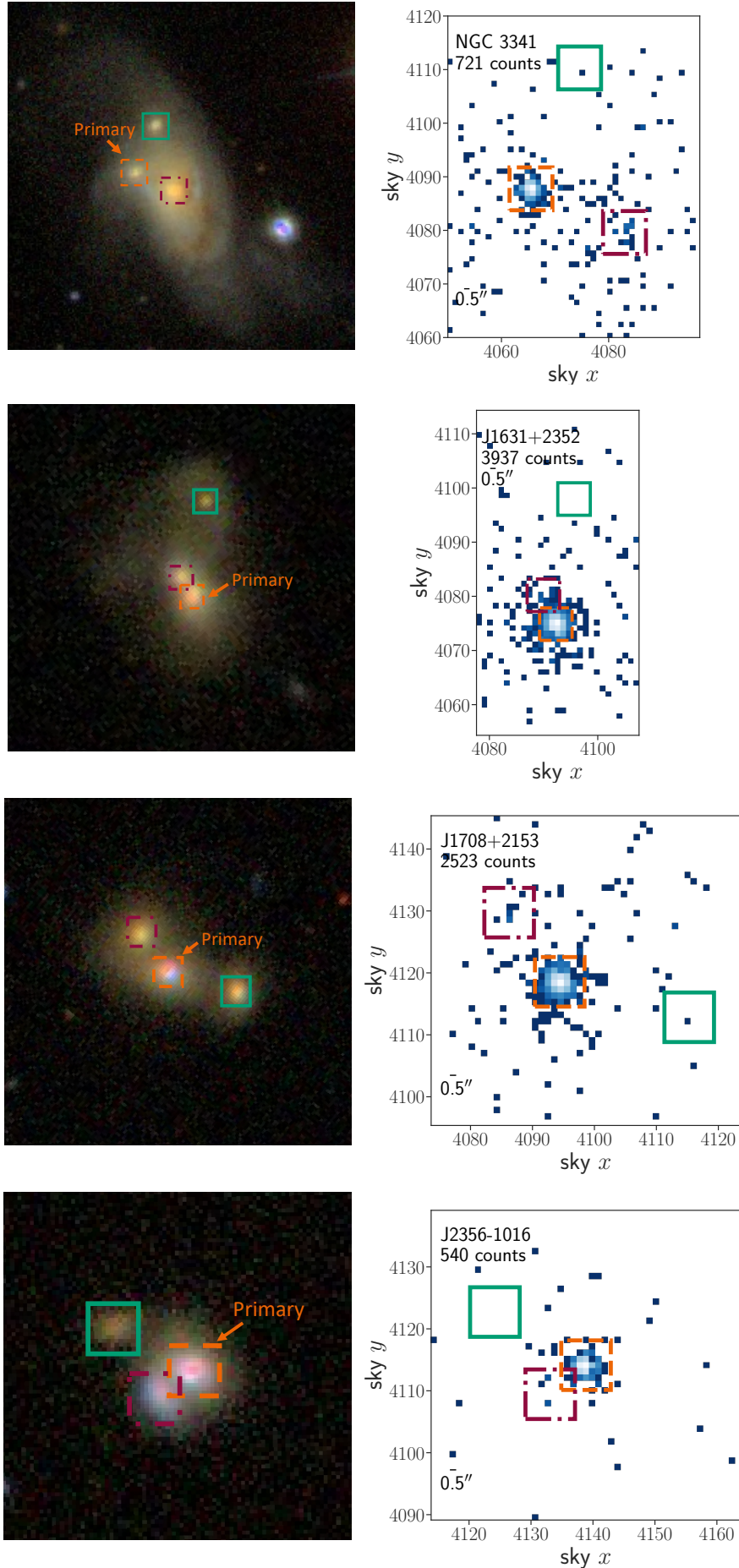


Figure 2. SDSS gri color composite observations (*left*), and *Chandra* 0.5–8 keV observations (*right*) of the triple mergers in our sample with no *HST* observations.

each observation we find the background flaring contribution to be negligible, with no time interval containing a background rate 3σ above the mean level.

Both SDSS J1708+2153 and SDSS J1631+2352 were observed in 1/8 sub-array mode to reduce pile-up. We quantify the levels of pile-up by running the CIAO tool `pileup_map` on both observations, which generates an output image with the number of counts per ACIS frame per pixel (these values can be converted to pile-up fractions; see Davis 2001). We find that both SDSS J1708+2153 and SDSS J1631+2352 reach pile-up fractions $< 5\%$ in the brightest pixel. Although both observations have visible read-out streaks, neither spatially intercept the locations of the other galaxies in each merger. The minimal pile-up and read-out streaks should have a negligible effect on our X-ray analysis.

3. METHODS

To analyze each *Chandra* observation for the presence of multiple X-ray point sources, we use BAYMAX (Bayesian Analysis of Multiple AGN in X-rays). BAYMAX is a tool designed to quantitatively evaluate whether a given *Chandra* observation is a single or multiple point source via a Bayesian framework (Foord et al. 2019, 2020). BAYMAX is especially powerful for systems with low count ratios between the AGN ($0.1 < f < 1.0$), and angular separations (r) below $0''.5$. For example, analyses on multiple AGN systems in the low- f and/or low- r regime without BAYMAX are likely to lead to false negatives/positives (e.g., Koss et al. 2015; Foord et al. 2020). With BAYMAX, we’ve analyzed many low count ratio dual AGN candidates, and are methodically expanding the small group of X-ray confirmed dual AGN (Foord et al. 2020).

In order to determine the likelihood of a given triple merger hosting multiple AGN, BAYMAX calculates the Bayes factor (hereafter denoted by \mathcal{B}). The Bayes factor represents the ratio of the marginal likelihood of two competing hypotheses. The value can be interpreted as a measure of the strength of evidence in favor of one hypothesis over the other. The Bayes factor can be defined mathematically as:

$$\mathcal{B}_{j/i} = \frac{\int P(D | \theta_j, M_j)P(\theta_j | M_j)d\theta_j}{\int P(D | \theta_i, M_i)P(\theta_i | M_i)d\theta_i} \quad (1)$$

Here, the marginal probability density of the observed data D under one model (M) is represented by $P(D | \theta, M)$, while each model is parameterized by a parameter vector, θ , and thus the prior densities are represented by $P(\theta | M)$. Regarding our X-ray analysis on the triple galaxy mergers, we calculate the evidence for three different models: a single point source model (i.e., the data

are consistent with the X-ray emission of a single AGN; M_1), a dual point source model (M_2), and a triple point source model (M_3). Thus, we calculate the Bayes factor twice, comparing the evidence of the dual point source model to that of the single point source model ($\mathcal{B}_{2/1}$), and the evidence of the triple point source model to the dual point source model ($\mathcal{B}_{3/2}$).

The main components of BAYMAX are as follows: (i) take calibrated *Chandra* events and compare them to the expected distribution of counts for single/multiple point sources models; (ii) calculate a Bayes factor to determine which model is preferred; (iii) calculate likely values for separations (r) and count ratios (f); and (iv) fit spectra to each model component. Regarding step (i), the probability densities of each model are estimated by comparing the sky coordinates (x, y) and energies (E) of each detected X-ray event to simulations based on single and multiple point source models.

The properties of the *Chandra* PSF are characterized by simulating the PSF of the optics with MARX (Davis et al. 2012). Testing has shown that the MARX PSF is more narrow than the *Chandra* PSF in real observations of point-like sources (testing was carried out using observations of TYC 8241 2652 1, a young star that was observed in 1/8 sub-array mode to reduce pile-up), where the effect is most pronounced at a radius of 1 sky pixel¹. At 1 pixel, the difference in the enclosed count fractions between the MARX and *Chandra* PSF is $\sim 10\%$. However, we’ve found that both in the low-count and wide-separation regime, the effect of these PSF differences is expected to be negligible. On top of this, all multiple AGN detected by BAYMAX in this study have separations larger than 1 sky pixel, such that differences in the MARX and *Chandra* PSF should not effect results.

For a source with multiple observations, BAYMAX first models the PSF of each observation and calculates the likelihoods for each observation individually (which is expected to depend on the detector position and start time of the observation), and then fits for astrometric shifts between different observations of the same source. Regarding step (ii) and (iii), BAYMAX uses nested sampling (Skilling 2004) to estimate the evidence of each model (via the PYTHON package `nestle`²) and uses PyMC3 (Salvatier et al. 2016) for parameter estimation. Below, we review the details of the prior densities used when running BAYMAX on observations of our triple galaxy merger sample. We refer the reader to Foord et al. (2019,

¹ <https://space.mit.edu/cxc/marx/tests/PSF.html>

² <https://github.com/kbarbary/nestle>

2020) for an in-depth review of the statistical techniques used to estimate likelihoods and posterior densities.

3.1. Prior Densities

For all models, each photon is assumed to originate from either a point source component or the background. Thus, M_1 is parameterized by vector $\theta_1 = [\mu, \log f_{bkg}]$, while M_2 and M_3 are parameterized by vector $\theta_{2,3} = [\mu_N, \log f_n, \log f_{bkg}]$. Here, μ_N represents the location for N point sources ($N = [1, \dots, N]$); f_{bkg} represents the ratio of counts between the background and the combined counts from all point source components; f_n represents the ratio of the total counts between a given point source and the primary point source ($n = [2, \dots, N]$), and in Fig. 1 we show which X-ray point source we classify as the primary. For the one system with multiple observations (SDSS J0849+1114, see Table 2), the parameter vectors additionally include Δx_k and Δy_k , which account for the translational components of the relative astrometric registration for the $k = [1, \dots, K-1]$ observation (where $K = 2$ for SDSS J0849+1114). For a single point source, the probability that a photon observed at sky coordinate (x, y) with energy E is described by the PSF centered at μ is $P(x, y | \mu, E)$, while for multiple point sources the total probability is $P(x, y | \mu_N, E, f_n, f_{bkg})$.

We assume that events associated with the background are uniformly distributed across a given region, such that the probability that a photon observed at location x, y on the sky with energy E is associated with a background component is $P(x, y | f_{bkg}, E)$. Because we assume that each background component is uniformly distributed, $P(x_i, y_i | f_{bkg}, E)$ is always constant over a given region of interest. With this current model, it is possible that a spatially uniform background with a higher count-rate sitting among a spatially uniform background with a lower count-rate can be mistaken for a resolved point source. Specifically, 2 of the 7 triple merger systems (SDSS J0858+1822 and SDSS J1027+1749), show evidence in their *Chandra* observations for a high-count, diffuse, emission surrounding the galactic nuclei (see Fig. 1). Extended, hot, gas is frequently detected in both simulations and observations of merging systems (see, e.g., Cox et al. 2006; Brassington et al. 2007; Sinha & Holley-Bockelmann 2009; Hopkins et al. 2013; Smith et al. 2018; Foord et al. 2020). For example, multiple analyses on dual AGN candidate SDSS J0841+0101 have found that the emission can be well-fit by two point sources (Comerford et al. 2015; Pfeifle et al. 2019b; Foord et al. 2020), but in Foord et al. (2020) we found that a uniform, high-count, distribution better explains the X-ray emission associated with sec-

ondary galactic nucleus, instead of point-like emission from an AGN. Thus, for SDSS J0858+1822 and SDSS J1027+1749 we add an additional background component to our model. In Figure 1 we show these additional regions of background components in gray regions, where the position and size of these regions are chosen such that they cover the majority of the optical emission of the triple galaxy merger, as determined from the SDSS DR16 observations. Within these regions, BAYMAX fits for a different background fraction, f_{diff} than for outside these regions.

All prior distributions of μ for all models are described by continuous uniform distributions. When using non-informative priors, the coordinates of each μ are allowed to be anywhere within a given region centered on the X-ray source centroid position; when using informative priors, the coordinates of each μ are defined by the locations of the galaxy nuclei as determined in the SDSS DR16 observations shown in Figure 1. We note that our informative prior distributions for μ are wide enough to account for the relative astrometric shifts between the *Chandra* and optical observations ($> 1''$). The prior distribution of $\log f_{bkg}$ is described by a truncated Gaussian distribution, $N(\mu_{bkg}, \sigma_{bkg}^2)$, where μ_{bkg} is estimated by evaluating the count-rate in 10 random and source-free regions within a $20''$ radius of the X-ray source centroid position. We set σ_{bkg} to 0.5, allowing for BAYMAX to easily move in parameter space, and we truncate $\log f_{bkg}$ at -3 and 0 . For M_2 and M_3 , the prior distributions of $\log f_n$ are described by uniform distributions and are constrained between -4 and 4 , accounting for a large range of possible count fractions between the X-ray emission of the AGN (and allowing for instances where the secondary or tertiary point source has more counts than the primary). For SDSS J0849+1114, the prior distributions of Δx_1 and Δy_1 are described by a uniform distribution constrained between $\delta\mu_{\text{obs}} - 3$ and $\delta\mu_{\text{obs}} + 3$, where $\delta\mu$ represents the difference between the observed central X-ray coordinates of two given observations. Here, we define Δx_k and Δy_k relative to the longest observation (ObsID: 18196). Lastly, for SDSS J0858+1822 and J1027+1749, the prior distribution of $\log f_{diff}$ is described by a uniform distribution constrained between -2 and 0 .

4. BAYES FACTOR RESULTS

For each observation, we restrict our analysis to photons with energies between 0.5–8 keV. We analyze the photons contained within rectangular regions that are centered on the midpoint of the nominal X-ray coordinates of the three point sources, μ_{obs} . The sky x - and y -lengths of each rectangle are defined as l_x and l_y , where

l_x and l_y vary between 20 and 60 sky-pixels for each observation (9.9" and 29.7", respectively; see Figure 1). Most analyses use square regions with $l_x=l_y$, however we use a rectangular region for our analysis of NGC 3341 to avoid the inclusion of a nearby, bright, X-ray source (not associated with the triple merger) and our analysis of SDSS J1631+2532 due to the large (~ 4000) number of 0.5–8 keV counts in the observation. In the latter case, this helps to lower the computational time (as the probability densities are calculated by summing the log probability of each individual X-ray event, and thus the computational time increases as a function of X-ray events analyzed). The known asymmetric *Chandra* PSF feature is within this extraction region (Juda & Karovska 2010), and sits approximately 0".7 from the center of the AGN. Because our PSF model does not take into account this asymmetry, we mask the feature in all exposures before running BAYMAX.

For each galaxy, we run BAYMAX using non-informative priors — where the prior distributions for μ are uniform distributions bound between $(\mu_{\text{obs}} - \frac{l_x}{2}, \mu_{\text{obs}} + \frac{l_x}{2})$ and $(\mu_{\text{obs}} - \frac{l_y}{2}, \mu_{\text{obs}} + \frac{l_y}{2})$ — and informative priors — where the distributions for μ are constrained by and centered on each galaxy in the triple merger system (see Figure 1). Here, the sky x and sky y limits of each prior distribution were determined by visually identifying the possible extent of a galactic nucleus via the optical observations.

Of the seven triple mergers, using informative priors, we find 1 that favors the triple X-ray point source model (SDSS J0849+1114), 5 that favor the dual X-ray point source model (SDSS J1027+1749, NGC 3341, SDSS J1631+2352, SDSS J1708+2153, SDSS J2356–1016) and 1 that favors the single point source model (SDSS J0858+1822). Here, if both $\ln \mathcal{B}_{1/2, \text{inform}}$ and $\ln \mathcal{B}_{3/2, \text{inform}}$ are consistent with 0, we classify the system as favoring the single point source model. In most cases where the Bayes factor favors a multi-point source model: (i) the Bayes factor favors the same model when using informative and non-informative priors, and (ii) the evidence for a given model is stronger when using informative priors. The one exception to this is SDSS J2356–1016, where the Bayes factor only favors the dual point source model when using informative priors. In Table 3 we list the various $\ln \mathcal{B}_{2/1}$ and $\ln \mathcal{B}_{3/2}$ values for each of the 7 triple merger systems.

The error bars on the Bayes factor represent the 99.7% confidence intervals, as determined by `nestle`. The errors provided by `nestle` are calculated for each model, at each iteration, and are assumed to be proportional to the ratio of the “information” (denoted H , and represents the logarithm of the fraction of prior mass that

contains the bulk of the posterior mass) to the number of live points (see Skilling 2004 for explicit details). We have found these errors to be consistent with the 3σ spread of the $\ln \mathcal{B}$ values when running BAYMAX multiple times on a single dataset.

4.1. Multiple X-ray Point Sources: Strength of the Bayes factor

For each triple merger that has a Bayes factor that favors either the triple or dual point source model, we run false-positive tests to better, and uniquely, define a “strong” Bayes factor. Past analyses have defined arbitrary Bayes factor thresholds, above which values are deemed strong (Jeffreys 1935, 1961; Kass & Raftery 1995). However, the interpretation of a strong Bayes factor value depends on the details of the dataset, and for our particular observations it depends on parameters such as the number of counts, count ratio, and separation.

Following the procedure outlined in Foord et al. (2019, 2020), for each system that has a Bayes factor favoring a model with multiple point sources, we simulate a suite of single point source simulations that are based on the *Chandra* observations. The simulations are created via MARX and use the same detector position, pointing, and exposure time of the *Chandra* observations (such that, on average, the point source will have the same number of counts as the primary point source). Additionally, the point source has the same spectrum as that of the primary point source. We only analyze the counts contained within the same sky coordinates and energy range as the observations, we use the same informative priors, and we add a uniform background contribution with a similar background fraction as each observation. For SDSS J1027+1749, we also add a synthetic diffuse emission component, constrained within the same region as shown in Fig. 1. For each system, we run BAYMAX on 100 such simulations and calculate what fraction have $\ln \mathcal{B}_{2/1} > 0$, or $\ln \mathcal{B}_{3/2} > 0$ (for the one triple point source system, SDSS J0849+1114).

For the false-positive runs based on SDSS J1027+1749, NGC 3341, SDSS J1631+2352, and SDSS J1708+2153, 0/100 of the $\ln \mathcal{B}_{2/1}$ values are larger than the measured values of 34.20, 2766.90, 6.20, and 18.40; for SDSS J2356–1016, only 2/100 of the $\ln \mathcal{B}_{2/1}$ values are larger than the measured value 3.10; while for SDSS J0849+1114, 0/100 of the $\ln \mathcal{B}_{3/2}$ values are larger than the measured value of 19.40. We interpret these results to mean that there is $\leq 99\%$ (or, $< 98\%$ for SDSS J2356–1016) chance that a single point source with a comparable number of counts would return a Bayes factor value, in favor of a multiple point source model,

Table 3. Bayes Factor Results

Galaxy Name	$\ln \mathcal{B}_{2/1}$	$\ln \mathcal{B}_{3/2}$	$\ln \mathcal{B}_{2/1,\text{inform}}$	$\ln \mathcal{B}_{3/2,\text{inform}}$
(1)	(2)	(3)	(4)	(5)
SDSS J0849+1114	23.4 ± 1.9	22.4 ± 2.1	25.6 ± 1.4	19.4 ± 1.9
SDSS J0858+1822	-2.3 ± 3.6	$2.1 \pm 3.8^\dagger$	0.6 ± 1.0	-0.8 ± 1.1
SDSS J1027+1749	28.5 ± 4.4	-4.5 ± 5.3	34.2 ± 1.8	-0.1 ± 1.9
NGC 3341	22.5 ± 1.8	$5.8 \pm 4.7^\dagger$	2766.9 ± 1.6	-0.1 ± 1.4
SDSS J1631+2352	2.7 ± 1.9	$2.3 \pm 3.8^\dagger$	6.2 ± 1.6	-0.8 ± 1.9
SDSS J1708+2153	16.6 ± 1.9	0.5 ± 3.9	18.4 ± 1.6	-1.9 ± 1.8
SDSS J2356-1016	0.7 ± 1.6	-0.9 ± 3.2	3.1 ± 1.3	-2.3 ± 1.4

Note. – Columns: (1) Galaxy name; (2) and (3) Bayes factor in favor of dual point source model and triple point source model, using non-informative priors on the locations (μ) of the point sources; (4) and (5) Bayes factor in favor of dual point source model and triple point source model, using informative priors on the locations (μ) of the point sources. Error bars represent the 99.7% confidence intervals. \dagger – Although $\ln \mathcal{B}_{3/2}$ favors the triple point source model for these systems, we emphasize that for SDSS J1027+1749 and SDSS J1631+2352 $\ln \mathcal{B}_{3/2}$ is consistent with 0 at the 99.7% C.L. For SDSS J1027+1749, the triple point source model is *not* favored over the single point source model i.e., $\ln \mathcal{B}_{3/1} \approx -0.15$. These results are likely due to clumpy, diffuse, X-ray emission, see section 5 for more details. For NGC 3341, $\ln \mathcal{B}_{3/2}$ weakly favors the triple point source model (when taking into account to the large error bars), again likely due to the presence of hot clumpy gas (see section 4).

greater than what we measure. Thus, we classify each Bayes factor value as “strong” in favor of the dual, or triple, point source model as indicated in Table 3.

5. X-RAY SPECTRAL ANALYSIS

In the following section we analyze the X-ray spectra of each point source individually, as well as analyze the posterior distributions returned from BAYMAX. For each system, we determine the best-fit values of each model parameter using the median values of their posterior distributions, which is appropriate given their unimodal nature. In Table 4 we list the best-fit values for r , θ_{PA} , $\log f$ and $\log f_{\text{bkg}}$. Here, θ_{PA} is the position angle between the primary and secondary (or, tertiary, for SDSS J0849+1114). All errors bars reported in this section are evaluated at the 99.7% confidence level, unless otherwise stated.

5.1. XSPEC Modeling

From our analysis in section 4, we find 5 triple merger systems with Bayes factors that strongly favor the dual point source model: SDSS J1027+1749, NGC 3341, SDSS J1631+2352, SDSS J1708+2153, SDSS J2356-1016; while we find one triple merger system with a Bayes factor that strongly favors the triple point source model: SDSS J0849+1114. As outlined in Foord et al. (2020), we use BAYMAX to carry out a spectral analysis of individual point source components in each observation. The spectral fits are determined via XSPEC, version 12.9.0 (Arnaud 1996). Each system has either 2 or 3 point sources, hereafter the “primary” (as defined in Fig. 1), “secondary”, or “tertiary”. We create 100 spectral realizations of each point source component by

probabilistically sampling from the full distribution of counts. Each spectral realization uses θ_2 or θ_3 values that are drawn from the posterior distributions as determined by BAYMAX. For each iteration, BAYMAX assigns each count to a specific model component, based on the relative probabilities of being associated with each component.

By fitting the 100 spectra of each point source component, we create distributions of the best-fit values for various spectral parameters, as well as the 0.5–8 keV flux and unabsorbed 2–7 keV luminosity. This additional analysis expands on the posterior distributions returned by BAYMAX, as fitting the spectral realizations for each point source results in estimates of the flux ratio, instead of the count ratio.

5.1.1. Fitting a Phenomenological Model

Similar to Foord et al. (2020), each point source component is modeled as either a simple absorbed power-law ($\text{phabs} \times \text{zphabs} \times \text{zpow}$; hereafter $m_{\text{phen},1}$) or an absorbed power-law with Compton scattering ($\text{phabs} \times (\text{pow} + \text{zphabs} \times \text{zpow})$; $m_{\text{phen},2}$), where the power-law indices are tied to one-another. We implement the Cash statistic (cstat ; Cash 1979) in order to best assess the quality of our model fits. Specifically, the latter model is used if it results in a statistically significant improvement in the fit, such that $\Delta C_{\text{stat}} > n \times 2.71$ (where n represents the difference in number of free parameters between the models; Tozzi et al. 2006; Brightman & Ueda 2012), corresponding to a fit improvement with 90% confidence (Brightman et al. 2014). Because we are evaluating distributions of spectral parameters, we require $\Delta C_{\text{stat}} > n \times 2.71$ at the

99.7% confidence level. For both $m_{\text{phen},1}$ and $m_{\text{phen},2}$, if the best-fitting model where Γ is free is a significantly better fit than the best-fitting model where Γ is fixed (fixed to a value of 1.8; Corral et al. 2011; Yan et al. 2015) we choose the model with Γ as free as the best-fitting model. Unsurprisingly, for point sources with a low number of average counts (< 20), the models where Γ is fixed tends to be a significantly better fit (Brightman & Ueda 2012). For each model, we fix the column density to the Galactic value (Kalberla et al. 2005) as well as the redshift to that of the host galaxy. We list the best-fit values for each spectral parameter, $F_{0.5-8}$, $L_{2-7 \text{ keV, unabs}}$, and hardness ratio (HR) in Table 5. The HR is defined as $(H - S)/(H + S)$ where H and S are the number of hard (2–8 keV) and soft (0.5–2 keV) X-ray counts. In Figures 6, 7, and 8 we show our various spectral fits to the spectral realizations of each X-ray point source.

5.1.2. Fitting a Physical Model

In addition to the aforementioned phenomenological model, we fit the spectral realizations that have, on average, over 100 counts between 0.5–8 keV (with the exception of the secondary in SDSS J0849+1114, which we also include and, on average, has 99 counts between 0.5–8 keV) using the physically motivated model **BNTorus** (Brightman & Nandra 2011). For a Compton thick AGN, a physical model may be able to better constrain parameters if the spectrum has a large-enough number of counts (~ 100 counts). We implement the **BNTorus** model in XSPEC, which considers an X-ray source surrounded by a toroidal structure (see Brightman & Nandra 2011 for more detail). Mirroring our analysis with the phenomenological model, we compare a simpler model ($m_{\text{phys},1}$, `phabs*atable[torus1006.fits]`) to a more complicated model that includes an additional scattered power-law component ($m_{\text{phys},2}$, `phabs*(s*pow+atable[torus1006.fits])`). Here, s is a constant and represents the scattering fraction of the additional power-law.

Similar to the `powerlaw` component in XSPEC, the toroidal component in **BNTorus** has parameters extragalactic N_H , photon index Γ , and redshift. Two additional parameters include the opening angle and the edge-on inclination of the torus; however we were unable to constrain either parameter during the spectral fits, and find that our results do not depend on their values. Thus, we fix them to default values of 60° and 87° . When using $m_{\text{phys},2}$, we tie the photon indices and normalizations between the power-law and toroidal component. For both models, we fix the column density to the Galactic value (Kalberla et al. 2005), the redshift to

that of the host galaxy, and allow each model to have both a fixed photon index ($\Gamma = 1.8$) as well as a photon index that is free to vary. We chose the most statistically significant model by analyzing the C_{stat} distributions between the fits.

For all sources, the best-fit model to describe the spectra are consistent between the phenomenological and physical XSPEC models; furthermore, the best-fit values for the parameters are consistent with one another. On average, however, the best-fit intrinsic absorption values found via the **BNTorus** toroidal model are slightly lower than those found via the phenomenological model. The exception to all of these results is the primary X-ray point source in NGC 3341, where a different model is favored when fitting with **BNTorus** ($m_{\text{phys},2}$, where the photon-index is fixed) than when using a phenomenological description ($m_{\text{phen},2}$, but the photon-index is free to vary). Furthermore, the best-fit intrinsic absorption value calculated by **BNTorus** is slightly larger than that calculated by the phenomenological model. Given that the primary X-ray point-source in NGC 3341 has one of the highest levels of obscuration, it is possible that fitting the spectral realizations for this source using a physically-motivated model will result in different, and better-constrained, model parameters.

Lastly, we measure whether the spectral fits via **BNTorus** over-fit data, which may occur when fitting lower count spectra. In this scenario, we may expect that the value of intrinsic absorption has little effect on the statistical significance of the fit. We analyze the χ_ν values for each system, using the best-fit model as described above, as well as the χ_ν values as a function N_H . In this latter case, we freeze the extragalactic N_H component, and step through parameter space ($-2 < \log N_H < 2$, where N_H is in units of 10^{22} cm^{-2}). For all spectra, we find best-fit χ_ν values between 0.85–1.05, where the two spectra with the lowest number of counts (SDSS J0849+114_p and SDSS J0849+114_s) have the two lowest χ_ν values, both below 1. However, when stepping through N_H parameter space, we find that all spectra have χ_ν values that strongly depend on N_H , where large deviations from the best-fit N_H value lead to large ($\gg 1$) χ_ν values. Thus, in the event that the physically motivated model is over-fitting the lower-count spectra, we don't expect that our estimates of N_H are affected. We list the best-fit values for each spectral parameter, $F_{0.5-8}$, and $L_{2-7 \text{ keV, unabs}}$ in Table 6.

5.1.3. Testing for Effects of Pileup

Lastly, for both SDSS J1708+2153 and SDSS J1631+2352, we investigate how pile-up possibly affects spectrum of

the primary X-ray point source. We convolve the spectral fits with the pile-up model implemented in XSPEC (Davis 2001), which accounts for the energy shifts due to photon pile-up as well as flux decrements due to grade migration. The pile-up model has six parameters: the CCD frame time, the maximum number of photons to pile-up, the grade correction for a single photon, the grade morphing parameter (which represents the probability, per photon count greater than one, that the piled event is not rejected by the spacecraft software as a “bad event”; thus the larger this parameter, the larger the effects of pile-up), the PSF fraction considered, and the number of event regions. Default values were assumed for the maximum number of photons to pile-up (5), the grade correction for a single photon (1), and the number of event regions (1). The frame time was set to that of the observation and the PSF fraction was set to 0.95. However, we find that the best-fit spectral parameter values are consistent with the values presented below, and thus conclude that any levels of pile-up have negligible effect on our spectral results.

Additionally, we note that SDSS J1708+2153 and SDSS J1631+2352 were both observed as part of the 70-month Swift/BAT all-sky survey, observations that are sensitive to the 14–195 keV energy range. This analysis combined available X-ray observations from a range of instruments, such as *XMM-Newton*, *Swift/XRT*, *ASCA*, *Chandra*, and *Suzaku*, to analyze the broadband X-ray (0.3–150 keV) characteristics of the AGN. We find that our X-ray spectral results agree with those presented in Ricci et al. (2017b), where the *Swift/XRT* observations of both AGN were not piled-up (see Sections 5.4 and 5.5). Thus, we conclude that any levels of pile-up have negligible effect on our spectral results.

5.1.4. Luminosity Estimates for Tertiary AGN

It is possible that additional X-ray point sources that either have low-luminosities within the *Chandra* energy band, and/or are highly-obscured will be undetected by BAYMAX. Thus, for systems with Bayes factors that favor the dual point source model, we estimate an upper-limit of the 2–7 keV luminosity of a possible tertiary X-ray point source. For a given set of parameter vectors θ_1 , θ_2 , and θ_3 , BAYMAX assigns each count to a specific model component (i.e., the primary, secondary, tertiary, or background), based on the relative probabilities of being associated with each component. Taking the best-fit values for θ_2 as determined by BAYMAX, we mask the counts associated with the primary and secondary point source, and analyze the counts within a $2''$ radius extraction region centered on the optical coordinates of the galactic nucleus found to host no X-ray

point source. We estimate the number of background-subtracted 0.5–8 keV counts associated with a possible tertiary, where the background contribution is estimated by evaluating the count-rate in 10 random and source-free regions, see section 3. These count rates are then converted into 2–7 keV luminosities via the HEASARC tool WebPIMMS (v4.11), assuming a power-law spectrum with photon index $\Gamma = 1.8$. We estimate the intrinsic luminosities assuming both a relatively unobscured system (with intrinsic $N_H = 1 \times 10^{20} \text{ cm}^{-2}$), as well as a system with a higher-level of absorption along the line-of-sight (with intrinsic $N_H = 1 \times 10^{22} \text{ cm}^{-2}$; such values are expected in merging environments, e.g., Ricci et al. 2017a; De Rosa et al. 2018; Koss et al. 2012; Hou et al. 2020).

5.2. SDSS J1027+1749

SDSS J1027+1749 was first identified as triple AGN candidate in Liu et al. (2011a). Optical [O III] $\lambda 5007$ luminosities were individually measured for each galactic nucleus using the Dual Imaging Spectrograph (DIS) on the Apache Point Observatory 3.5 m telescope. Assuming each galaxy hosts an AGN, X-ray luminosities were estimated from the $\frac{L_{X,2-10\text{keV}}}{L_{\text{[OIII]}}}$ relation for obscured AGN (Panessa et al. 2007). The estimated 2–10 keV luminosities for each AGN were all estimated to be greater than $10^{42} \text{ erg s}^{-1}$, representing a robust classification as a triple AGN system. However, the *Chandra* observation presents a more complicated scenario — a high-count, diffuse, emission is coincident with the primary galactic nucleus, and very little X-ray emission appears to coincide with the location of the western galaxy. Our analysis with BAYMAX, where we can include more complicated models that include various background regions, is necessary in order to understand whether the X-ray emission is consistent with three AGN.

BAYMAX finds the observation to have a Bayes factor that strongly favors the dual point source model, both with informative ($\ln \mathcal{B}_{2/1,\text{inform}} = 34.2 \pm 1.8$) and non-informative ($\ln \mathcal{B}_{2/1} = 28.5 \pm 4.4$) priors. Furthermore, the locations of the primary and secondary point source are consistent between the informative and non-informative runs, and spatially coincide with the optical nuclei of the primary and northern-most galaxy. We find the best-fit values of separation and count ratio to be $r = 3.4_{-0.3}^{+0.4}$ and $\log f = -0.1_{-0.4}^{+0.5}$. Thus, the separation is inconsistent with 0 at the 99.7% confidence level. In Figure 3 we show the best-fit locations of each point source and the joint posterior distribution for r and $\log f$.

Running our spectral analysis on the primary and secondary point source, we find that the primary and sec-

ondary have, on average, 37 and 35 counts. Both X-ray point sources are best-fit with $m_{\text{phen},1}$ where Γ is fixed to a value of 1.8. For the primary, we calculate a total observed 0.5–8 keV flux of $5.7_{-1.6}^{+1.3} \times 10^{-15}$ erg s $^{-1}$ cm $^{-2}$, while for the secondary we calculate a total observed 0.5–8 keV flux of $4.8_{-2.2}^{+1.1} \times 10^{-15}$ erg s $^{-1}$ cm $^{-2}$ s $^{-1}$. This corresponds to a rest-frame 2–7 keV luminosity of $3.2_{-0.9}^{+0.8} \times 10^{40}$ erg s $^{-1}$ and $2.6_{-1.2}^{+0.6} \times 10^{40}$ erg s $^{-1}$ at $z = 0.066$. Since we have fixed both point sources to have the same spectral shape, the count ratio that we calculate with BAYMAX, should represent the flux ratio between the two sources. We find that the log of the flux ratio calculated via XSPEC (≈ -0.07) is consistent with the posterior distribution of $\log f$ (where the median value corresponds to $\log f \approx -0.1$).

Lastly, we estimate an upper-limit of the 2–7 keV luminosity of a possible tertiary X-ray point source at the location of the western galaxy. We find 0_{-0}^{+1} background-subtracted 0.5–8 keV counts within the nucleus of the SW galaxy, (where errors bars represent the 99% C.L. as determined by Poisson statistics, see Gehrels 1986). Assuming a power-law spectrum with photon index $\Gamma = 1.8$, we estimate the upper-limit on L_X to be between 1.50×10^{39} erg s $^{-1}$ (if intrinsic $N_H = 1 \times 10^{20}$ cm $^{-2}$) and 2.36×10^{39} erg s $^{-1}$ (if intrinsic $N_H = 1 \times 10^{22}$ cm $^{-2}$).

5.3. NGC 3341

The first analysis of NGC 3341 was presented in Barth et al. (2008), where SDSS data and new observations from the Keck Observatory were analyzed. Results from optical diagnostics were deemed too ambiguous for a proper classification of the AGN-nature of each galaxy. Expanding on this study via a multi-wavelength analysis that combined optical, X-ray, and radio data, Bianchi et al. (2013) concluded that the primary galaxy showed evidence for AGN activity. Although the SW nucleus had emission detected in almost every wave-band, the emission was consistent with star-formation ($L_{2-7, \text{keV}} \approx 4 \times 10^{39}$ erg s $^{-1}$, while there was no sign of any compact source at 5 GHz).

Our analysis with BAYMAX results in a Bayes factor that strongly favors the dual point source model, both with informative ($\ln \mathcal{B}_{2/1, \text{inform}} = 2766.9 \pm 1.6$) and non-informative priors ($\ln \mathcal{B}_{2/1} = 22.5 \pm 1.8$). The locations of the primary and secondary point source are consistent between the informative and non-informative runs, and spatially coincide with the optical nuclei of the primary and SW galaxy. We find the best-fit values of separation and count ratio to be $r = 9.6_{-0.4}^{+0.3}$ and $\log f = -1.6_{-0.4}^{+0.4}$. Although we find that the system weakly (given the large error bars) favors the triple point source model, over the dual point source model,

when using non-informative priors ($\ln \mathcal{B}_{3/2} = 5.8 \pm 4.7$), this is interpreted to be due to the presence of hot gas in the vicinity of the primary and secondary galactic nuclei; this emission is seen both in the SDSS and *Chandra* observations. BAYMAX finds the best-fit location of the “tertiary” in a clumpy X-ray emission region south east of the secondary point source, spatially inconsistent with any galactic nucleus. In Figure 3 we show the best-fit locations of each point source and the joint posterior distribution for r and $\log f$.

Running our spectral analysis on the primary and secondary point source, we find that the primary and secondary have, on average, 566 and 16 counts. The primary X-ray point source is best-fit with $m_{\text{phen},2}$, where Γ is free to vary; while the secondary X-ray point source is best-fit with $m_{\text{phen},1}$ where Γ is fixed to a value of 1.8. The primary in NGC 3341 is the only source that shows inconsistencies between our phenomenological and physically-motivated spectral fits. In particular, we find that when using BNTorus the primary X-ray point sources is best-fit with $m_{\text{phys},2}$ where Γ is fixed to a value of 1.8. As such, we list the parameters for both models below (and refer the reader to Tables 5 and 6). Additionally, we note that the main difference between our X-ray spectral analysis and that presented in Bianchi et al. 2013, is that Bianchi et al. 2013 fit the spectrum of the primary in NGC 3341 with a single power-law (analogous to $m_{\text{phen},1}$ in our analysis). They find the best-fit model one where the power-law photon index is fixed to a value of $\Gamma = 1.7$ (due to not being able to constrain the value in the fit).

For the primary, when using the phenomenological model, we calculate a total observed 0.5–8 keV flux of $3.63_{-0.05}^{+0.07} \times 10^{-13}$ erg s $^{-1}$ cm $^{-2}$, corresponding to a rest-frame 2–7 keV luminosity of $8.54_{-0.33}^{+0.41} \times 10^{41}$ erg s $^{-1}$ at $z = 0.027$. The spectrum of the primary is measured to have extragalactic $N_H = 1.0 \pm 0.06 \times 10^{23}$ cm $^{-2}$, with a relatively flat photon index of $\Gamma = 1.1_{-0.1}^{+0.1}$. The high level of N_H and flat spectral shape is consistent with an obscured environment. When using the physically motivated model, where Γ is kept fixed at a value of 1.8, we calculate a total observed 0.5–8 keV flux of $1.39_{-0.01}^{+0.01} \times 10^{-12}$ erg s $^{-1}$ cm $^{-2}$, corresponding to a rest-frame 2–7 keV luminosity of $1.18_{-0.01}^{+0.02} \times 10^{42}$ erg s $^{-1}$ at $z = 0.027$. The intrinsic absorption is measured to be slightly higher ($N_H = 1.2_{-0.02}^{+0.01} \times 10^{23}$ cm $^{-2}$) than the value determined using $m_{\text{phen},2}$.

For the secondary, we calculate a total observed 0.5–8 keV flux of $2.7_{-0.8}^{+0.6} \times 10^{-15}$ erg s $^{-1}$ cm $^{-2}$ s $^{-1}$. This corresponds to a rest-frame 2–7 keV luminosity of $2.3_{-0.7}^{+0.9} \times 10^{39}$ erg s $^{-1}$ at $z = 0.027$. Although the primary has an X-ray luminosity consistent with accretion onto an AGN

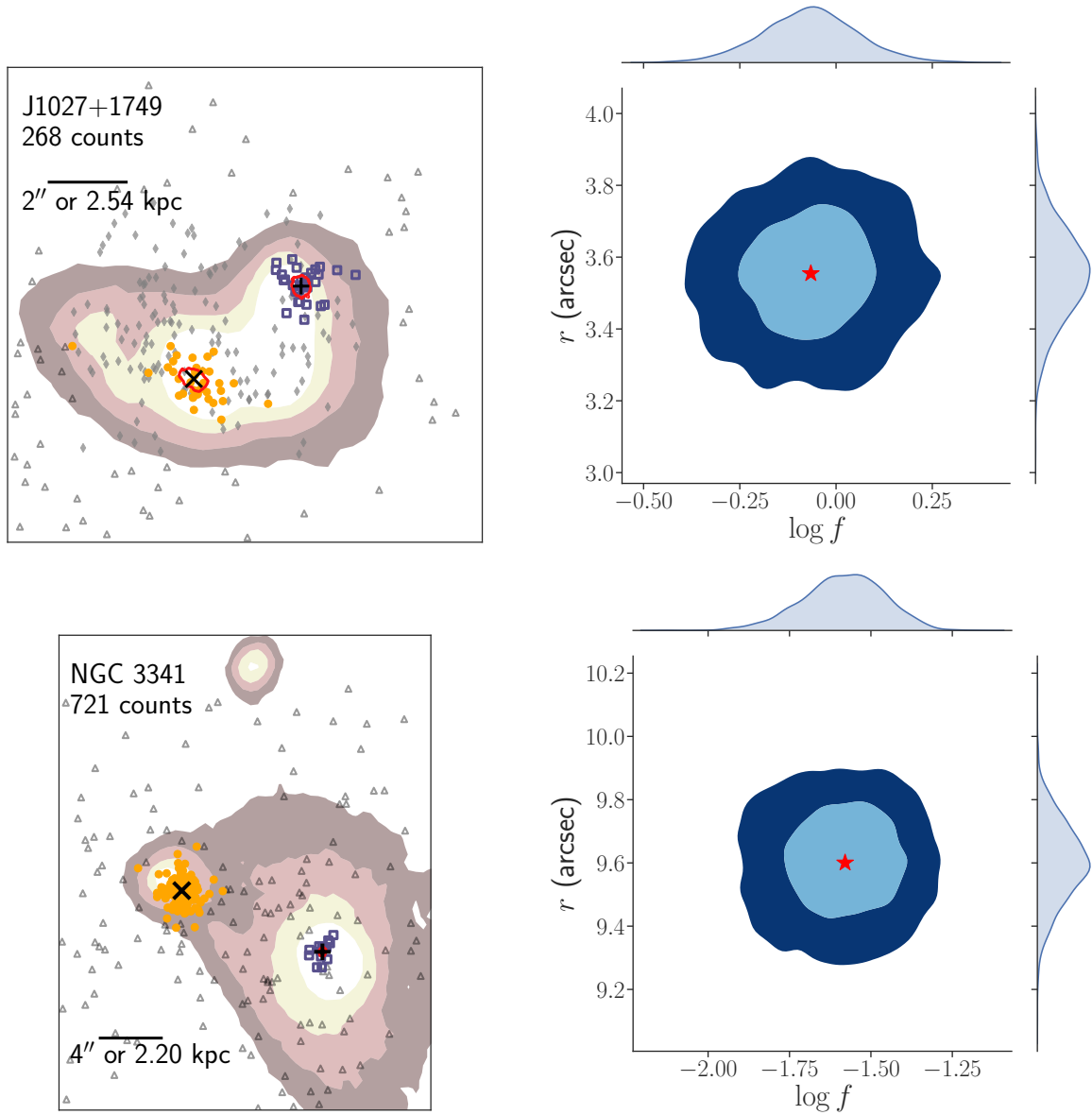


Figure 3. The 0.5–8 keV datasets for the two dual AGN candidates SDSS J1027+1749 and NGC 3341 (*left*) and their joint posterior distributions for r and $\log f$ (*right*). In the left panels, we plot the 68% confidence intervals (red lines) for the best-fit (as determined by BAYMAX) sky x and sky y positions for a primary and secondary (which are smaller than the symbol in most instances). Here, counts most likely associated with the primary are denoted by yellow circles, counts most likely associated with the secondary are denoted by open-faced purple squares, and counts most likely associated with background are shown as open-faced gray triangles. In order to more clearly see the results, we do not bin the data. Contours of the SDSS i-band observations of the host galaxies are overplotted in brown. In the right panels, we show joint posterior distribution for the separation r (in arcseconds) and the count ratio (in units of $\log f$), with the marginal distributions shown along the border. The 68%, and 95% confidence intervals are shown in light and dark blue contours, respectively. We denote the location of the median of the posterior distributions with a red star.

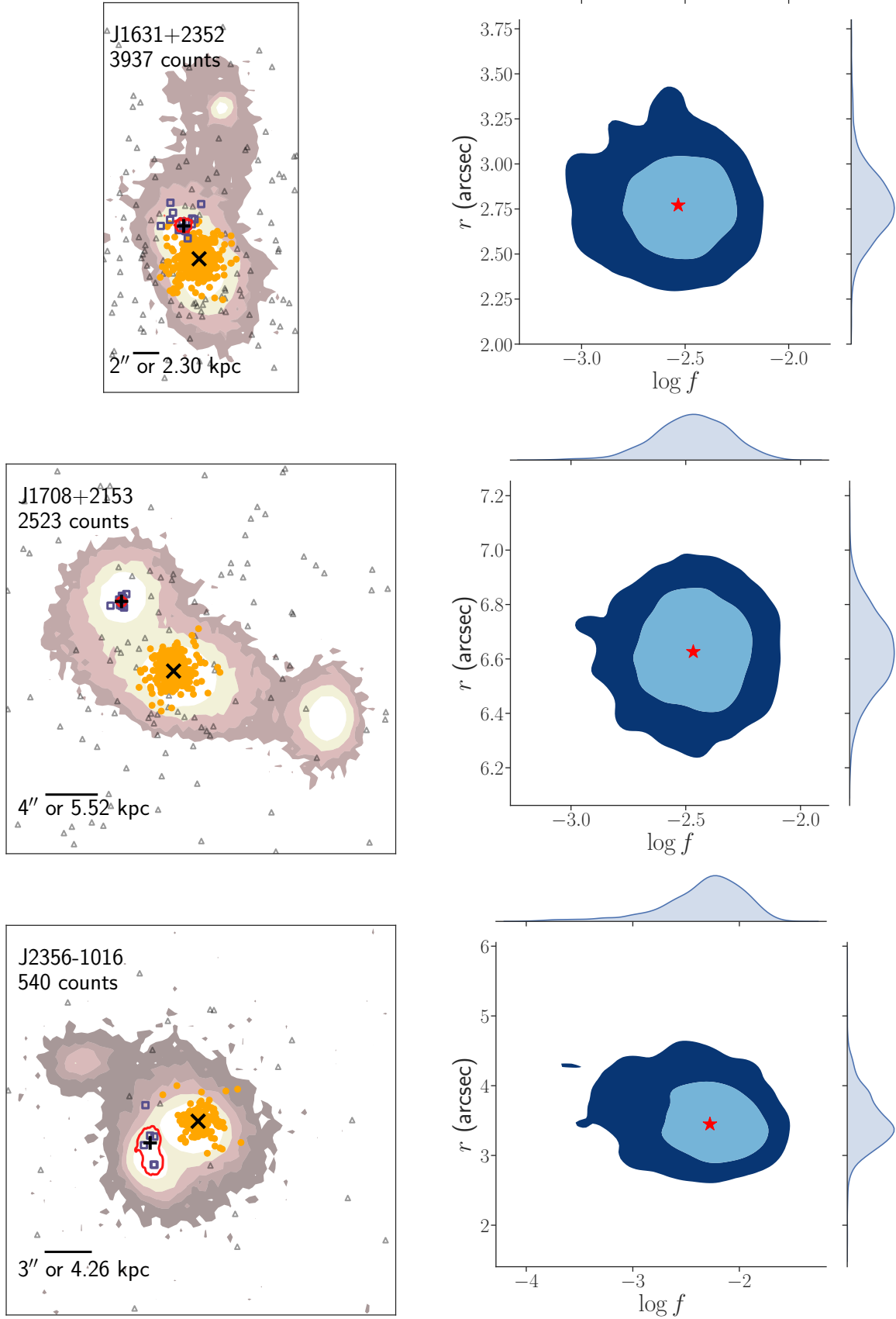


Figure 4. The 0.5–8 keV datasets for the three dual AGN candidates J1631+2352, SDSS J1708+2153 and SDSS J2356–1016 (left) and their joint posterior distributions for r and $\log f$ (right). Symbols and contours follow the same guidelines as Fig. 3

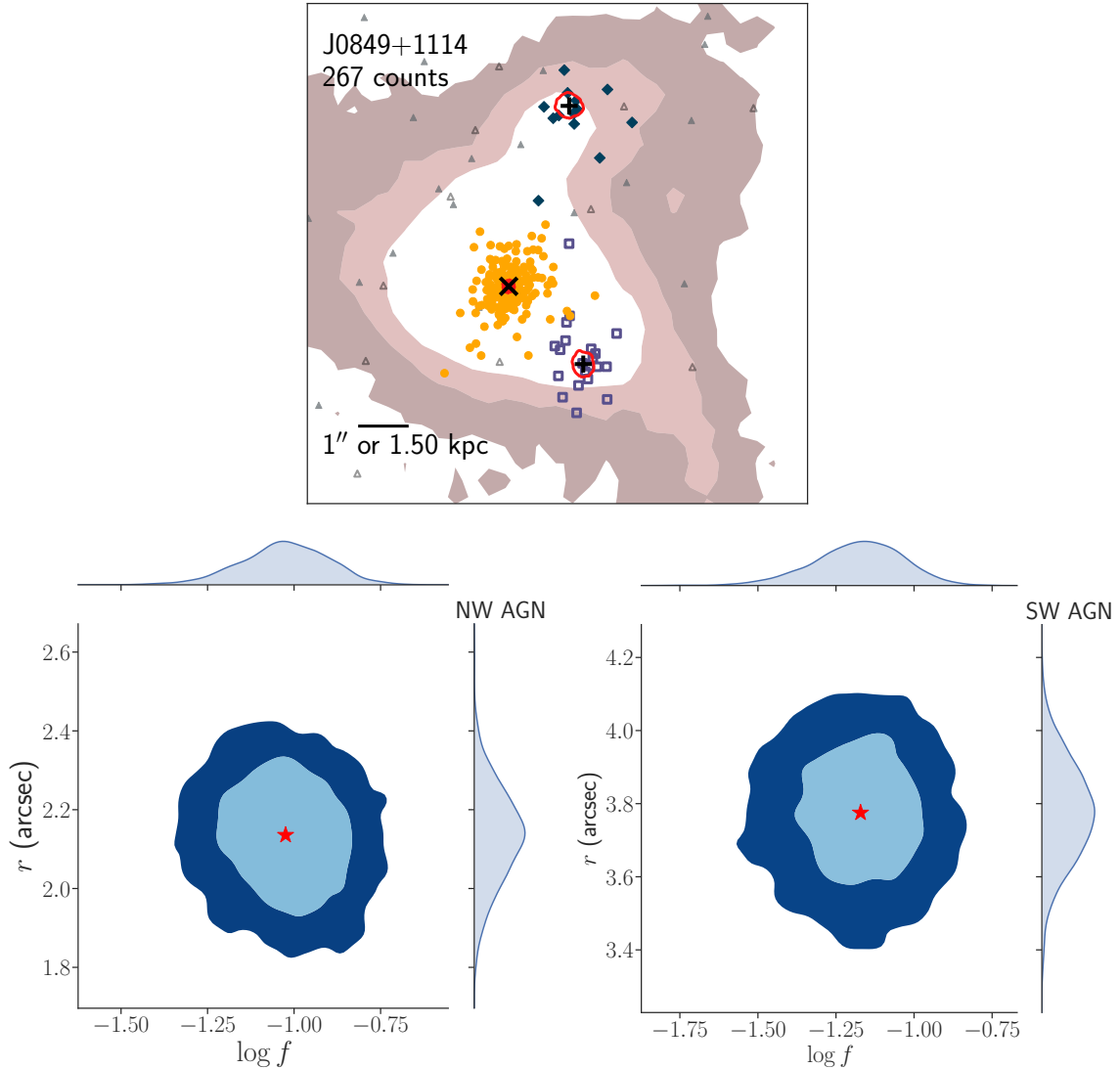


Figure 5. The 0.5–8 keV datasets for the triple AGN SDSS J0849+1114 (*top*) and the joint posterior distributions for r and $\log f$ for the secondary and tertiary X-ray point sources (*bottom*). Symbols and contours follow the same guidelines as Fig. 3, while we denote the counts most likely associated with the tertiary point source with green filled diamonds.

(regardless of spectral model used, $L_X > 1 \times 10^{41}$ erg s^{-1}), the SW galaxy does not ($L_X < 1 \times 10^{40}$ erg s^{-1}). These results agree with what was previously found in Bianchi et al. (2013).

We estimate an upper-limit on the 2–7 keV luminosity of possible tertiary X-ray point source at the location of the NW galaxy. We find 0_{-0}^{+1} 0.5–8 keV background-subtracted counts within the nucleus of the NW galaxy. Assuming a power-law spectrum with photon index $\Gamma = 1.8$, we estimate the upper-limit on L_X to be between 1.80×10^{39} erg s^{-1} (if intrinsic $N_H = 1 \times 10^{20}$ cm^{-2}) and 2.86×10^{39} (if intrinsic $N_H = 1 \times 10^{22}$ cm^{-2}).

5.4. SDSS J1631+2352

SDSS J1631+2352 is a triple merger system at $z = 0.059$, with no previous analysis on the *Chandra* data

beyond fitting the nuclear X-ray spectra associated with the primary galaxy (Ricci et al. 2017a). It was observed as a part of a study on mergers in the *Swift* BAT AGN sample (Koss et al. 2010; Ricci et al. 2017a). Analyzing the archival *Chandra* observation with BAYMAX, we find that the data favor the dual point source model when using both informative ($\ln \mathcal{B}_{2/1, \text{inform}} = 2.7 \pm 1.9$) and non-informative priors ($\ln \mathcal{B}_{2/1} = 6.2 \pm 1.6$). The best-fit value for the separation between the two point sources is $r = 2.8_{-0.6}^{+1.3}$, inconsistent with 0 at the 99.7% confidence level; furthermore the best-fit location of the secondary point source is consistent with the location of the NE galaxy using both informative and non-informative priors. The best-fit value for count ratio is $\log f = -2.5_{-0.5}^{+0.4}$. We show the best-fit locations of each

point source, and the joint posterior distributions for r and $\log f$ in Figure 4.

The spectral realizations of the primary (with an average of 3810 counts) and secondary (with an average of 11 counts) point source are best-fit with $m_{\text{phen},2}$ and $m_{\text{phen},1}$, with Γ fixed to a value of 1.8. When fitting the spectral realizations of the primary point source, we identify a statistically significant Fe K α fluorescent emission line, modeled by a Gaussian component (`zgauss`) fixed at 6.4 keV. We measure an equivalent width of $0.23^{+0.01}_{-0.02}$ keV for the Fe K α line. The equivalent width of the Fe K α line is strongly dependent on line-of-sight absorption, as well as other parameters such as geometry of the accretion disk, inclination angle at which the reflecting surface is viewed, and the elemental abundances of the reflecting matter (see, e.g., [Brightman & Nandra 2011](#)). Although we measure a relatively mild line-of-sight hydrogen column density when fitting the 0.5–8 keV spectrum for the primary ($N_H = 1.10^{+0.01}_{-0.02} \times 10^{22}$ cm $^{-2}$), analysis of the available *NuSTAR* observations (which are above 10 keV), may better constrain the spectral parameters (e.g., [Marchesi et al. 2018](#)). However, past analyses of the *Swift* BAT observations (sensitive to the 15–150 keV energy range) of the merger conclude similar levels of obscuration, with $N_H = 5.0^{+1.6}_{-3.0}$, using more complicated spectral models ([Ricci et al. 2017b](#)). We calculate a total observed 0.5–8 keV flux of $2.29^{+0.01}_{-0.01} \times 10^{-12}$ erg s $^{-1}$ cm $^{-2}$, and $5.3^{+4.8}_{-3.9} \times 10^{-15}$ erg s $^{-1}$ cm $^{-2}$ for the primary and secondary, respectively. These flux values are consistent with the extrapolated 2–7 keV flux measurements from the *Swift* BAT observations [Ricci et al. \(2017b\)](#). They correspond to rest-frame 2–7 keV luminosities, at $z = 0.059$, of $1.33^{+0.01}_{-0.01} \times 10^{43}$ erg s $^{-1}$ and $2.5^{+2.3}_{-1.8} \times 10^{40}$ erg s $^{-1}$.

We estimate the upper-limit of the 2–7 keV luminosities of a possible tertiary X-ray point source at the location of NW host-galaxy nuclei. We find 0^{+1}_{-0} 0.5–8 keV counts associated with a possible tertiary (NW galaxy) in SDSS J1631+2352. Assuming a power-law spectrum with photon index $\Gamma = 1.8$, we estimate the upper-limit on L_X to be between 3.19×10^{39} erg s $^{-1}$ (if intrinsic $N_H = 1 \times 10^{20}$ cm $^{-2}$) and 4.89×10^{39} (if intrinsic $N_H = 1 \times 10^{22}$ cm $^{-2}$).

5.5. SDSS J1708+2153

SDSS J1708+2153 is a triple merger system at $z = 0.072$. Similar to SDSS J1631+2352, it was observed as a part of a study on mergers in the *Swift* BAT AGN sample ([Koss et al. 2010](#); [Ricci et al. 2017a](#)), and the *Chandra* observations have no previous analysis beyond fitting the nuclear X-ray spectra associated with the primary galaxy ([Ricci et al. 2017a](#)). Analyzing the archival

Chandra observations with BAYMAX, we find that the data strongly favor the dual point source model when using both informative ($\ln \mathcal{B}_{2/1, \text{inform}} = 18.4 \pm 1.6$) and non-informative priors ($\ln \mathcal{B}_{2/1} = 16.6 \pm 1.9$). The best-fit value for the separation is $r = 6.6^{+0.4}_{-0.4}$, inconsistent with 0 at the 99.7% confidence level, while the best-fit value for count ratio is $\log f = -2.5^{+0.4}_{-0.6}$. We show the best-fit locations of each point source, and the joint posterior distributions for r and $\log f$ in Figure 4. The best-fit location for the secondary is coincident with the location of the NE galaxy, using both informative and non-informative priors.

Analyzing the spectral realizations of each point source, we find that the primary and secondary have, on average, 2406 and 9 counts. Both the primary and secondary point sources are best-fit with $m_{\text{phen},1}$, where Γ is allowed to vary for the primary. For the primary, we calculate a total observed 0.5–8 keV flux of $1.46^{+0.01}_{-0.01} \times 10^{-12}$ erg s $^{-1}$ cm $^{-2}$, while for the secondary we calculate a total observed 0.5–8 keV flux of $4.6^{+1.6}_{-0.2} \times 10^{-15}$ erg s $^{-1}$ cm $^{-2}$. Once again, these flux measurements are consistent with what was found in [Ricci et al. \(2017a\)](#), when analyzing the *Swift* BAT spectrum. Our measured flux values correspond to rest-frame 2–7 keV luminosities of $1.17^{+0.01}_{-0.01} \times 10^{43}$ erg s $^{-1}$ and $3.5^{+0.6}_{-1.2} \times 10^{40}$ erg s $^{-1}$ at $z = 0.072$. The spectral fit of the primary point source shows low-levels of absorption, with $N_H = 0.10^{+0.01}_{-0.01} \times 10^{22}$ cm $^{-2}$ and best-fit photon index $\Gamma = 1.37^{+0.01}_{-0.01}$.

Lastly, we estimate an upper-limit of the 2–7 keV luminosity of a possible tertiary X-ray point sources at the location of the SW galaxy. Subtracting the expected background contribution, we find 0^{+1}_{-0} 0.5–8 keV counts associated with the nucleus of the SW galaxy. Assuming a power-law spectrum with photon index $\Gamma = 1.8$, we estimate the upper-limit on L_X to be between 4.80×10^{39} erg s $^{-1}$ (if intrinsic $N_H = 1 \times 10^{20}$ cm $^{-2}$) and 7.15×10^{39} (if intrinsic $N_H = 1 \times 10^{22}$ cm $^{-2}$).

5.6. SDSS J2356–1016

SDSS J2356–1016 was analyzed in [Pfeifle et al. \(2019b\)](#), where they concluded that the X-ray emission was consistent with a single AGN. They find an X-ray detection at the location of the primary galaxy (at the 22.8σ C.L.), but they find no X-ray detection at the location of the SE galaxy, which is separated from the primary by $3.5''$. However, source detection was determined using the CIAO package `wavdetect`, which is not always sensitive enough to detect both low-count and closely-separated multiple point source systems (see, e.g., [Foord et al. 2020](#)). Given that BAYMAX is a power-

ful tool for low count systems, we re-analyze this triple merger to identify any previously missed detections.

Analyzing the archival *Chandra* observations with BAYMAX, we find that the data strongly favor the dual point source model when using informative priors ($\ln \mathcal{B}_{2/1,\text{inform}} = 3.1 \pm 1.3$). The Bayes factor does not strongly favor the dual point source model when using non-informative priors, likely due to the low number of counts associated with the secondary point source; however the best-fit locations of the primary and secondary point source are consistent between non-informative and informative runs, and spatially coincide with the primary and SE galaxy. During our false positive tests, only 2 out of 100 simulations of single point sources analyzed by BAYMAX have $\ln \mathcal{B}_{2/1,\text{inform}} > 3$, and thus we classify the merger as a dual X-ray point source system. The best-fit values of separation and count ratio are $r = 3.5_{-1.2}^{+1.6}$ and $\log f = -2.4_{-1.5}^{+0.7}$. This separation is inconsistent with 0 at the 99.7% confidence level. We show the best-fit locations of each point source, and the joint posterior distributions for r and $\log f$ in Figure 4.

Analyzing the spectral realizations of each point source, we find that the primary and secondary have, on average, 516 and 4 counts. The primary point source is best-fit with $m_{\text{phen},2}$ while the secondary point source is best-fit with $m_{\text{phen},1}$ where Γ is fixed for both models. We calculate a total observed 0.5–8 keV flux of $1.60_{-0.01}^{+0.01} \times 10^{-12}$ erg s $^{-1}$ cm $^{-2}$ for the primary, while for the secondary we calculate a total observed 0.5–8 keV flux of $7.3_{-3.5}^{+7.0} \times 10^{-15}$ erg s $^{-1}$ cm $^{-2}$ s $^{-1}$. This corresponds to a rest-frame 2–7 keV luminosity of $3.11_{-0.04}^{+0.04} \times 10^{43}$ erg s $^{-1}$ and $8_{-1}^{+10} \times 10^{40}$ erg s $^{-1}$ at $z = 0.074$. The spectral fit of the primary point source shows relatively high (with respect to the other dual X-ray point sources in the sample) levels of absorption, with $N_H = 7.8_{-0.1}^{+0.2} \times 10^{22}$ cm $^{-2}$.

We estimate an upper-limit of the 2–7 keV luminosity of possible tertiary X-ray point sources at the location of the NE galaxy. We find 0_{-0}^{+1} 0.5–8 keV background-subtracted counts associated with the nucleus of the NE galaxy. Assuming a power-law spectrum with photon index $\Gamma = 1.8$, we estimate the upper-limit on L_X to be between 1.02×10^{40} erg s $^{-1}$ (if intrinsic $N_H = 1 \times 10^{20}$ cm $^{-2}$) and 1.50×10^{40} (if intrinsic $N_H = 1 \times 10^{22}$ cm $^{-2}$).

Although our analysis and false positive tests for SDSS J2356–1016 show the weakest evidence for a dual X-ray source, the detected secondary has the hardest X-ray spectrum of all our the systems in our sample. Follow-up observations with either optical and/or IR IFU will help reveal the true origin of X-ray emission.

5.7. SDSS J0849+1114

SDSS J0849+1114 is a triple AGN candidate first published by Pfeifle et al. (2019b), and in-depth analyses followed in Pfeifle et al. (2019a) and Liu et al. (2019). Pfeifle et al. (2019b) conclude that the primary is detected at a 10.2σ level, while the SW and NE galaxy are detected at 2.2σ and 1.4σ , respectively. Given the lower significance of the SW and NE detections, we re-evaluate the system with BAYMAX to determine the likelihood that the merger is composed of three X-ray point sources. We find that BAYMAX strongly favors the triple point source system using both informative ($\ln \mathcal{B}_{3/2,\text{inform}} = 19.4 \pm 1.9$) and non-informative priors ($\ln \mathcal{B}_{3/2} = 22.4 \pm 2.1$); furthermore the locations of each point-source are consistent between the informative and non-informative runs, and spatially coincide with the optical nuclei of each galaxy in the triple merger. The best-fit values for the separation and count ratio of the secondary (associated with the SW galaxy) X-ray point source are $r = 2.1_{-0.3}^{+0.3}$ and $\log f = -1.0_{-0.4}^{+0.4}$, while the best-fit values for separation and count ratio of the tertiary (associated with the NW galaxy) X-ray point source are $r = 3.8_{-0.4}^{+0.4}$ and $\log f = -1.2_{-0.5}^{+0.4}$. Here, the separation and count-ratio are defined relative to the position and number of counts associated with the primary point source. These separations are inconsistent with 0 at the 99.7% confidence level. We show the best-fit locations of each point source, and the joint posterior distributions for r and $\log f$ in Figure 5.

Creating 100 spectral realizations of each point source, we find that the primary, secondary, and tertiary have, on average, 189, 99, and 13 counts. The primary point source source is best-fit with $m_{\text{phen},2}$ where Γ is fixed to a value of 1.8, while the secondary and tertiary point sources are best-fit with $m_{\text{phen},1}$ where Γ is fixed to value of 1.8. Although Pfeifle et al. (2019b) find that adding an Fe K α emission component into the primary’s spectral model results in statistically significant better fit (using only one of the two *Chandra* observations), we find that the combined *Chandra* dataset results in spectral realizations that do not favor the addition of an Fe K α emission component (and a similar conclusion was reached in Pfeifle et al. 2019a when combining all available observations from *Chandra* and *NuSTAR*). We calculate a total observed 0.5–8 keV fluxes of: $6.54_{-0.22}^{+0.28} \times 10^{-14}$ erg s $^{-1}$ cm $^{-2}$ for the primary; $4.0_{-1.3}^{+1.6} \times 10^{-15}$ erg s $^{-1}$ cm $^{-2}$ for the secondary; and $3.2_{-1.3}^{+1.0} \times 10^{-15}$ erg s $^{-1}$ cm $^{-2}$ for the tertiary. This corresponds to rest-frame 2–7 keV luminosities (at $z = 0.059$) of: $1.60_{-0.40}^{+0.80} \times 10^{42}$ erg s $^{-1}$ for the primary, $1.9_{-0.7}^{+0.6} \times 10^{40}$ erg s $^{-1}$ for the secondary, and $1.3_{-0.5}^{+0.6} \times 10^{40}$ erg s $^{-1}$ for the tertiary. The spectral fit of the primary point source

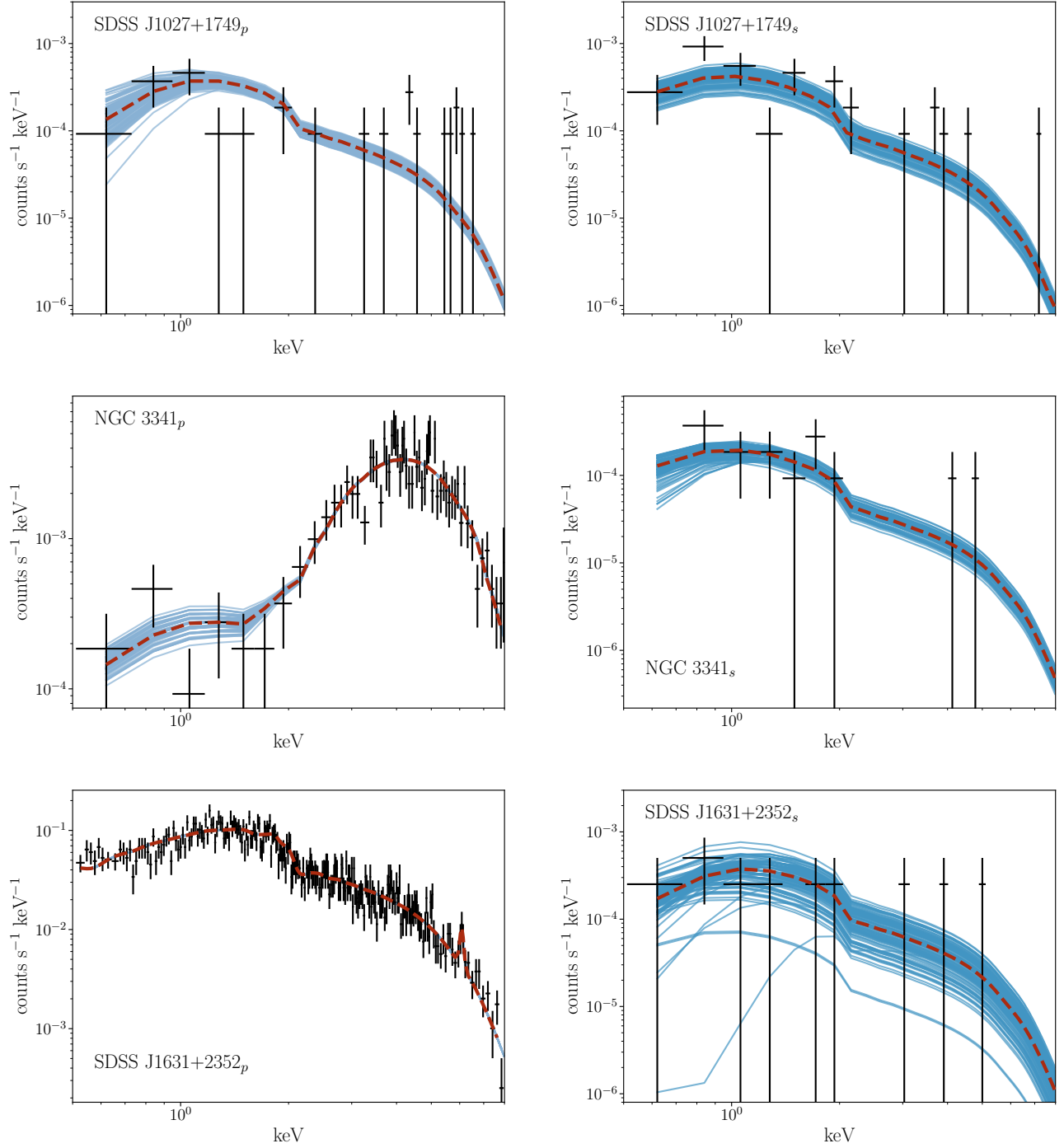


Figure 6. X-ray spectral fits of 100 realizations for the primary point source (*left*) and the secondary point source (*right*) in SDSS J1027+1749, NGC 3341, and SDSS J1631+2352. Data have been folded through the instrument response. We overplot one of the spectral realizations in black and the median spectral fit in a red dashed line. The spectra have been rebinned for plotting purposes. We list the best-fit values for each model in Table 5, defined as the median of the distribution of the best-fit values from the 100 realizations.

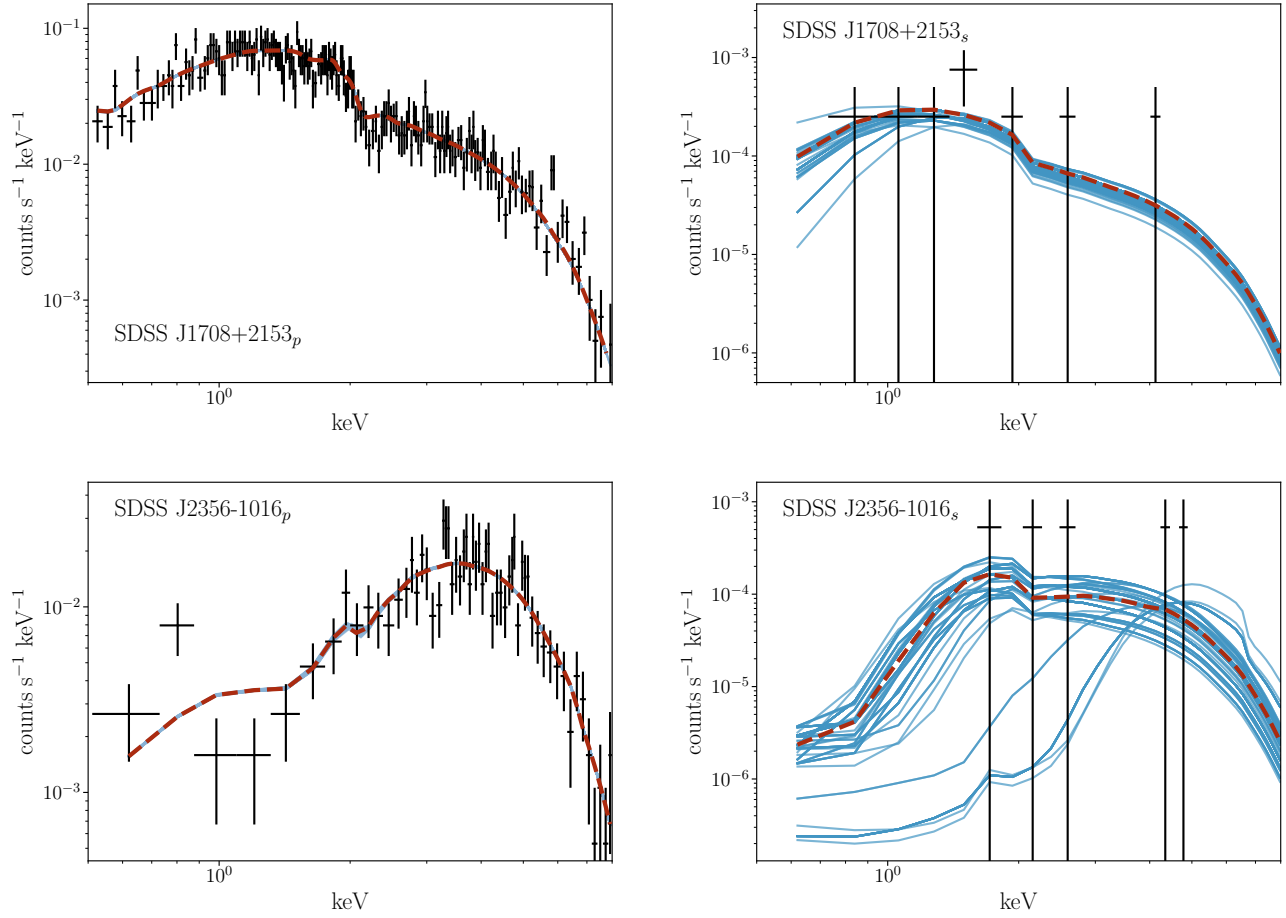


Figure 7. *Chandra* spectral fits of 100 realizations for the primary (*left*) and secondary (*left*) X-ray point sources in SDSS J1708+2153 and SDSS J2356-1016. Plotting symbols and lines follow the the same guidelines as Fig. 6.

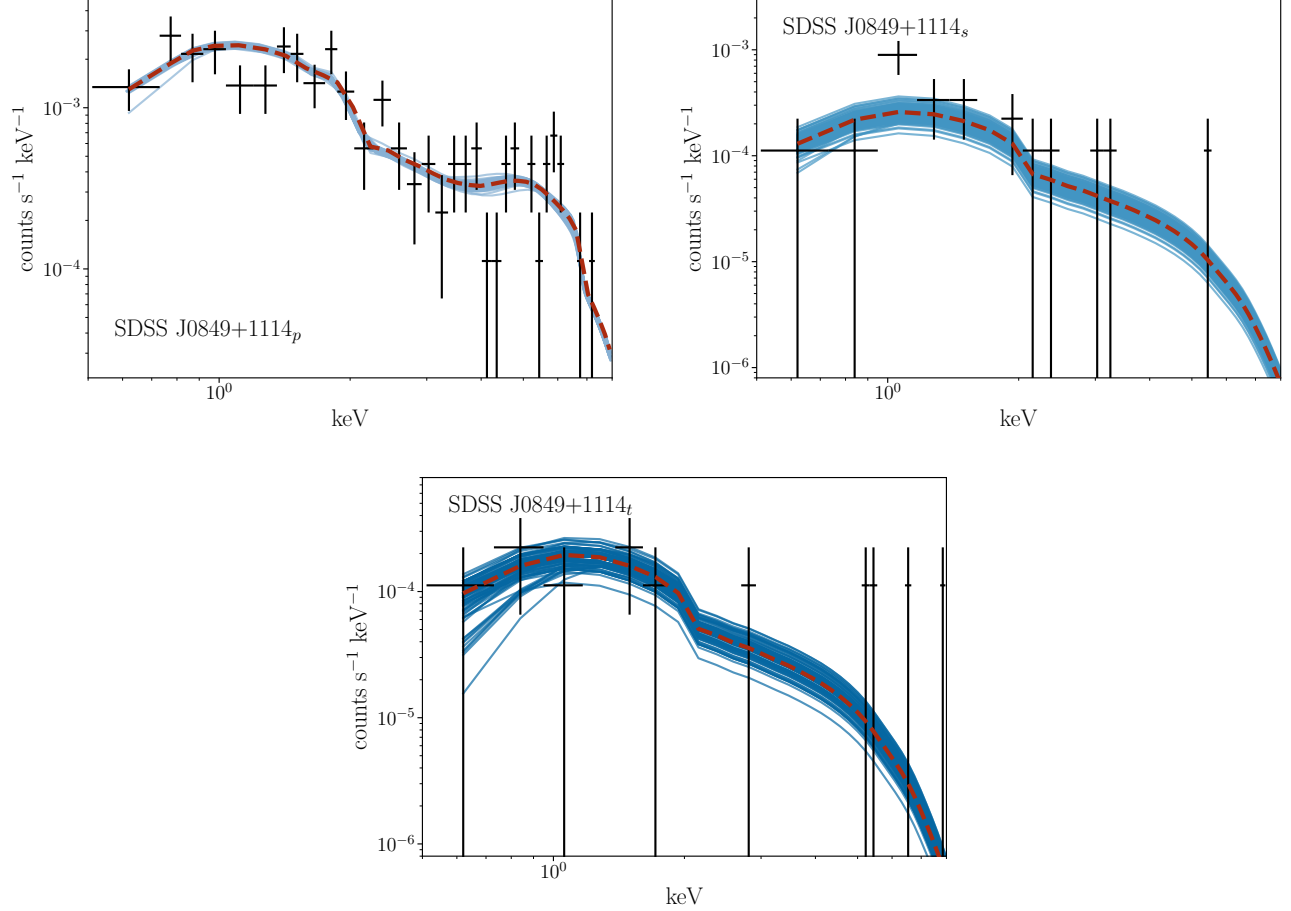


Figure 8. *Chandra* spectral fits of 100 realizations for the primary (*top left*), secondary (*top right*), and tertiary (*bottom*) X-ray point sources in SDSS J0849+1114. Plotting symbols and lines follow the the same guidelines as Fig. 6.

shows one of the highest-levels of absorption in our sample, with $N_H = 5.2^{+2.3}_{-1.1} \times 10^{23} \text{ cm}^{-2}$.

5.8. SDSS J0858+1822: Clumpy Diffuse Emission or Compton Thick AGN

SDSS J0858+1822 is a unique system within our sample, where there appears to be an excess of X-ray emission south of the primary galaxy (see Fig. 1), which does not spatially coincide with a galactic nucleus. Interestingly, when using non-informative priors, BAYMAX favors the single point source model, but with the best-fit location for the point source corresponding to the location of the southern region of X-ray emission. This is consistent with our results when running BAYMAX with informative priors – the single point source model is favored, but the location of the point source is shifted to the southern-most edge of the spatial constraints placed on μ . These results are complementary to the results of the optical analysis presented in Husemann et al. (2020), where the [O III] emission-line peak was found to be offset by $1''$ from the position of the primary galactic

nucleus. We aim to better understand the accretion nature of the southern emission region (which, for example, may be explained by a background AGN or a recoiling SMBH), and do so by analyzing the spectrum.

We use the results from the non-informative run to create 100 spectral realizations of the point source south of the primary galaxy; this is done by sampling from the posterior distributions of θ_1 and probabilistically assigning counts to either the point source or background component. The spectral realizations of the point source are best-fit with $m_{\text{phen},1}$ where Γ is free to vary. We calculate a total observed 0.5–8 keV flux of $3.0^{+2.6}_{-1.3} \times 10^{-15} \text{ erg s}^{-1} \text{ cm}^{-2}$, corresponding to a rest-frame 2–7 keV luminosity of $2.1^{+0.1}_{-0.1} \times 10^{39} \text{ erg s}^{-1}$ at $z = 0.077$. The region is extremely soft, with best-fit $\Gamma = 8.5^{+0.7}_{-5.4}$ and $HR = -0.9^{+0.4}_{-0.1}$. These results can be well-explained by a concentrated region (or, clump) of the surrounding diffuse emission, that is better modeled as a point-source sitting among a uniform background.

The very soft emission can possibly originate from an AGN if the system is Compton thick; here, all emis-

sion above 10 keV is absorbed, and the observed 2–8 keV X-ray emission is a result of the reflected and reprocessed (such as from narrow-line regions; see, e.g., Liu et al. 2013; Comerford et al. 2015) emission. In such a scenario, the intrinsic X-ray luminosity can be ~ 60 – 70 times higher with respect to what is observed (corresponding to an X-ray luminosity on the order of 10^{41} erg s $^{-1}$, compatible with an AGN; e.g., Panessa et al. 2006; Lamastra et al. 2009; Marinucci et al. 2012). We test this hypothesis by fitting the spectrum of the southern source in SDSS J0858+1822 with $m_{\text{phen},1}$, fixing the photon index of the power-law to 1.8, and calculating the expected value of intrinsic N_H . Doing so, we find that best-fit $N_H < 1 \times 10^{-20}$ cm $^{-2}$. However, an additional complication to this analysis is that Compton-thick sources may appear to have low-levels of absorption if using simple models and/or low-count data sets (Risaliti et al. 1999). Thus, deeper *Chandra* X-ray observations, or observations with instruments that are more sensitive to harder X-rays (such as XMM and / or NuSTAR), and/or multi-wavelength follow-up (i.e., optical/IR spectroscopy and/or radio observations) can potentially help constrain the origin of X-ray emission.

5.9. Classifications of X-ray Point Sources

In general, bona fide AGN can usually be classified as point sources with unabsorbed 2–7 keV luminosities $L_{2-7 \text{ keV,unabs}} > 10^{41}$ erg s $^{-1}$, while likely AGN are classified as point sources with unabsorbed 2–7 keV luminosities $L_{2-7 \text{ keV,unabs}} > 10^{40}$ erg s $^{-1}$. Any point source with $L_{2-7 \text{ keV,unabs}} < 10^{40}$ erg s $^{-1}$ is conservatively not classified as an AGN.

The main source of contamination are X-ray binaries (XRBs) or ultraluminous X-ray sources (ULXs); however, most high-mass X-ray binary (HMXBs) have 2–7 keV X-ray luminosities between 10^{38} – 10^{39} erg s $^{-1}$, while the ULX population dominates at the highest luminosities, with $L_{2-7 \text{ keV}} > 10^{39}$ erg s $^{-1}$ (e.g., Swartz et al. 2011; Walton et al. 2011). The overall X-ray luminosity function (XLF) of HMXBs and ULXs indicates a general cutoff at $L_{2-7 \text{ keV}} = 10^{40}$ erg s $^{-1}$ (e.g., Mineo et al. 2012; Sazonov & Khabibullin 2017; Lehmer et al. 2019), and previous studies on XRB contamination in both late- and early-type galaxies have concluded that the majority of nuclear (within $2''$ of the galactic nucleus) X-ray point sources with $L_{2-7 \text{ keV}} > 10^{40}$ erg s $^{-1}$ are highly unlikely to be emission associated with accretion onto XRBs (Foord et al. 2017a; Lehmer et al. 2019). However, these studies have yet to focus on a sample of merging galaxies, where amplified star formation rates can increase the surrounding X-ray emission. Thus, from our X-ray data alone, we can safely clas-

sify any system with unabsorbed 2–7 keV luminosities $L_{2-7 \text{ keV,unabs}} > 10^{41}$ erg s $^{-1}$ as an AGN. However, each point source with $10^{40} < L_{2-7 \text{ keV,unabs}} < 10^{41}$ erg s $^{-1}$, will need a separate and more detailed analysis using complementary IR observations in order to estimate the expected X-ray contribution from high-mass X-ray binaries. We defer this facet of the analysis to a separate paper analysing the multi-wavelength emission of each triple galaxy merger.

Thus, from our spectral analysis alone (see Table 5) we can classify NGC 3341 as a single AGN system; while SDSS J161+2352, SDSS J1708+2153, SDSS J2356–1016, and SDSS J0849+1114 have at least one AGN (the primary point source in all cases). We note that these other dual X-ray point source systems all have primary and secondary point sources with bright X-ray luminosities ($L_{2-7\text{keV}} > 10^{40}$ erg s $^{-1}$), possibly associated with 4 new undetected dual AGN. A multi-wavelength analysis is required for a better understanding of the true duality, or triality, of all these systems.

6. CONCLUSIONS

In this study, we present the first X-ray analysis of AGN activity in triple galaxy mergers. We analyze 7 nearby ($0.059 < z < 0.077$) triple galaxy mergers with existing archival *Chandra* and SDSS DR16 observations. Each of these systems are confirmed as triple mergers with available spectroscopic and/or photometric redshift measurements. Running BAYMAX on these observations, we aim to detect low-count and closely-separated multiple AGN systems. Archival SDSS DR16 and/or *HST* observations allow for informative priors on the locations of each AGN, while BAYMAX allows for a statistical analysis on the presence of an X-ray point source at each galactic nucleus. The main results of this study are summarized below:

1. We find that 1 triple merger system favors the single point source model (SDSS J0858+1822); 5 triple merger systems favor the dual point source model (SDSS J1027+1749, NGC 3341, SDSS J1631+2352, SDSS J1708+2153, and SDSS J2356–1016); and one triple merger system favors the triple point source model (SDSS J0849+1114). All of the multiple point source systems have Bayes factors that favor the same model when using both informative and non-informative priors, with the exception of SDSS J2356–1016, which has a Bayes factor that favors the dual point source model only when using informative priors.

Table 4. Posterior Results for Multiple X-ray Point Sources

Galaxy Name	α	δ	α_s	δ_s	r (arcsec)	θ_{PA} (degrees)	$\log f$	$\log f_{bkg}$
(1)	(2)	(3)	(4)	(5)	(6)	(7)	(8)	(9)
SDSS J1027+1749	10:27:00.39	+17:49:02.94	10:27:00.57	+17:49:00.63	$3.4^{+0.4}_{-0.3}$	-130^{+8}_{-8}	$-0.1^{+0.5}_{-0.4}$	$-0.2^{+0.1}_{-0.1}$
NGC 3341	10:42:31.46	+05:02:37.94	10:42:32.05	+05:02:41.75	$9.6^{+0.3}_{-0.4}$	114^{+3}_{-4}	$-1.6^{+0.4}_{-0.4}$	$-0.7^{+0.1}_{-0.1}$
SDSS J1631+2352	16:31:15.52	+23:52:57.62	16:31:15.60	+23:53:00.10	$2.8^{+1.3}_{-0.6}$	-23^{+20}_{-25}	$-2.5^{+0.4}_{-0.5}$	$-1.5^{+0.1}_{-0.1}$
SDSS J1708+2153	17:08:59.12	+21:53:08.06	17:08:59.41	+21:53:13.33	$6.6^{+0.4}_{-0.4}$	-37^{+4}_{-5}	$-2.5^{+0.4}_{-0.6}$	$-1.4^{+0.1}_{-0.1}$
SDSS J2356–1016	23:56:54.36	–10:16:05.45	23:56:54.56	–10:16:06.77	$3.5^{+1.6}_{-1.2}$	-113^{+14}_{-41}	$-2.4^{+0.7}_{-1.5}$	$-1.4^{+0.3}_{-0.4}$
SDSS J0849+1114	08:49:05.54	+11:14:47.94	08:49:05.44	+11:14:46.42	$2.1^{+0.3}_{-0.3}$	137^{+8}_{-10}	$-1.0^{+0.4}_{-0.4}$	$-0.8^{+0.2}_{-0.2}$
...	$08:49:05.46^\dagger$	$+11:14:51.49^\dagger$	$3.8^{+0.4^\dagger}_{-0.4}$	$18.8^{+6.1}_{-7.7}$	$-1.2^{+0.4^\dagger}_{-0.5}$	–

Note. – Columns: (1) SDSS galaxy designation; (2) the central R.A. of the primary X-ray source; (3) the central declination of the primary X-ray source; (4) the central R.A. of the secondary X-ray source; (5) the central declination of the secondary X-ray source; (6) the separation between the two point sources in arcseconds; (7) the position angle between the primary and secondary, measured East of North; (8) the log of the count ratio between the secondary and primary; (9) the log of the count ratio between the background and point source contribution. The dagger represents posterior results for the tertiary point source in SDSS J0854+1114. For SDSS J1027+1749, the background component is defined as the diffuse emission component, f_{diff} . Each value is the best-fit value from the posterior distributions, defined as the median of the distribution. All posterior distributions are unimodal, and thus the median is a good representation of the value with the highest likelihood. Error bars represent the 99.7% confidence level of each distribution.

Table 5. Best-fit Spectral Parameters for Phenomenological Model

Galaxy Name	$m_{\text{phen},x}$	N_H (10^{22} cm $^{-2}$)	Γ	$F_{0.5-8}$ keV	L_{2-7} keV, unabs	HR
(1)	(2)	(3)	(4)	(5)	(6)	(7)
SDSS J1027+1749 _p	1	$< 10^{-2}$	1.8	$5.7^{+1.3}_{-1.6}$	$3.2^{+0.8}_{-0.9}$	$0.1^{+0.2}_{-0.4}$
SDSS J1027+1749 _s	1	$< 10^{-2}$	1.8	$4.8^{+1.1}_{-2.2}$	$2.6^{+0.6}_{-1.2}$	$-0.1^{+0.2}_{-0.4}$
NGC 3341 _p	2	$10.1^{+0.5}_{-0.6}$	$1.1^{+0.1}_{-0.1}$	$363.0^{+7.0}_{-5.6}$	$85.4^{+4.1}_{-3.3}$	$0.8^{+0.1}_{-0.1}$
NGC 3341 _s	1	$< 10^{-2}$	1.8	$2.7^{+0.6}_{-0.8}$	$0.2^{+0.1}_{-0.1}$	$-0.5^{+0.2}_{-0.5}$
SDSS J1631+2352 _p	2	$1.10^{+0.01}_{-0.02}$	1.8	$2.29^{+0.01}_{-0.01} \times 10^3$	$1.33^{+0.01}_{-0.01} \times 10^3$	$0.15^{+0.01}_{-0.01}$
SDSS J1631+2352 _s	1	$0.13^{+2.26}_{-0.01}$	1.8	$5.3^{+4.8}_{-3.9}$	$2.5^{+2.3}_{-1.8}$	$0.0^{+0.3}_{-0.7}$
SDSS J1708+2153 _p	1	$0.10^{+0.01}_{-0.01}$	$1.4^{+0.1}_{-0.1}$	$1.46^{+0.01}_{-0.01} \times 10^3$	$1.17^{+0.01}_{-0.01} \times 10^3$	$-0.02^{+0.01}_{-0.01}$
SDSS J1708+2153 _s	1	$0.2^{+0.5}_{-0.1}$	1.8	$4.6^{+0.2}_{-1.6}$	$3.5^{+0.6}_{-1.2}$	$-0.4^{+0.2}_{-0.2}$
SDSS J2356–1016 _p	2	$7.8^{+0.2}_{-0.1}$	1.8	$1.60^{+0.01}_{-0.01} \times 10^3$	$3.11^{+0.04}_{-0.04} \times 10^3$	$0.73^{+0.01}_{-0.01}$
SDSS J2356–1016 _s	1	$3.2^{+1.1}_{-0.1}$	1.8	$7.3^{+7.0}_{-3.5}$	8^{+10}_{-1}	$0.6^{+0.4}_{-0.5}$
SDSS J0849+1114 _p	2	52^{+23}_{-11}	1.8	$65.4^{+2.8}_{-2.2}$	160^{+80}_{-40}	$0.34^{+0.05}_{-0.04}$
SDSS J0849+1114 _s	1	$< 10^{-2}$	1.8	$4.0^{+1.6}_{-1.3}$	$1.9^{+0.6}_{-0.7}$	$-0.2^{+0.3}_{-0.2}$
SDSS J0849+1114 _t	1	$< 10^{-2}$	1.8	$3.2^{+1.0}_{-1.3}$	$1.3^{+0.6}_{-0.5}$	$0.0^{+0.3}_{-0.2}$

Note. – Columns: (1) SDSS galaxy designation, we denote the primary, secondary, and tertiary with subscripts p , s , and t ; (2) the spectral model used; (3) the best-fit extragalactic column density; (4) the assumed or best-fit spectral index; (5) the measured 0.5–8 keV flux, in units of 10^{-15} erg s $^{-1}$ cm $^{-2}$; (6) the rest-frame, unabsorbed, 2–7 keV luminosity in units of 10^{40} erg s $^{-1}$; (7) the hardness ratio, defined as $(H - S)/(H + S)$. Each best-fit value is defined as the median of the full distribution. We identify a statistically significant Fe K α fluorescent emission line in the spectrum of SDSS J1631–1016_p, modeled by a Gaussian component (**zgauss**) fixed at 6.4 keV, with an equivalent width of $0.23^{+0.01}_{-0.02}$ keV (see Fig. 6). Error bars represent the 99.7% confidence level of each distribution.

Table 6. Best-fit Spectral Parameters for BNTorus

Galaxy Name (1)	$m_{\text{phys},x}$ (2)	s (%) (3)	N_H (10^{22} cm $^{-2}$) (4)	Γ (5)	$F_{0.5-8}$ keV (6)	L_{2-7} keV, unabs (7)
NGC 3341 _p	2	0.19 $^{+0.07}_{-0.06}$	11.8 $^{+0.2}_{-0.2}$	1.8	1.39 $^{+0.01}_{-0.01}$ $\times 10^3$	118.2 $^{+1.6}_{-1.3}$
SDSS J1631+2352 _p	2	35.72 $^{+0.50}_{-0.40}$	0.99 $^{+0.01}_{-0.02}$	1.8	2.29 $^{+0.01}_{-0.01}$ $\times 10^3$	1.38 $^{+0.01}_{-0.01}$ $\times 10^3$
SDSS J1708+2153 _p	1	–	0.09 $^{+0.1}_{-0.01}$	1.38 $^{+0.01}_{-0.01}$	1.46 $^{+0.01}_{-0.01}$ $\times 10^3$	1.17 $^{+0.01}_{-0.01}$ $\times 10^3$
SDSS J2356–1016 _p	2	1.13 $^{+0.01}_{-0.02}$	7.0 $^{+0.1}_{-0.1}$	1.8	1.61 $^{+0.01}_{-0.01}$ $\times 10^3$	3.18 $^{+0.03}_{-0.04}$ $\times 10^3$
SDSS J0849+1114 _p	2	10.6 $^{+3.5}_{-2.8}$	46 $^{+14}_{-11}$	1.8	66 $^{+8}_{-6}$	160.6 $^{+21.1}_{-10.0}$
SDSS J0849+1114 _s	1	–	$< 10^{-2}$	1.8	4.0 $^{+1.6}_{-1.2}$	1.8 $^{+0.7}_{-0.6}$

Note. – Columns: (1) SDSS galaxy designation, we denote the primary, secondary, and tertiary with subscripts p , s , and t ; (2) the spectral model used; (3) the scattering fraction of the additional power-law; (4) the best-fit extragalactic column density; (5) the assumed or best-fit spectral index; (6); the measured 0.5–8 keV flux, in units of 10^{-15} erg s $^{-1}$ cm $^{-2}$; (7) the rest-frame, unabsorbed, 2–7 keV luminosity in units of 10^{40} erg s $^{-1}$. Each best-fit value is defined as the median of the full distribution. In agreement with our phenomenological fits, we identify a statistically significant Fe K α fluorescent emission line in the spectrum of SDSS J1631–1016_p, modeled by an additional Gaussian component (**zgauss**) fixed at 6.4 keV, with an equivalent width of 0.23 $^{+0.02}_{-0.01}$ keV. Error bars represent the 99.7% confidence level of each distribution. HR values for each system are independent of model, and are listed in Table 5 for each X-ray point source.

2. We quantify the strength of the Bayes factor, by running false positive tests. We find that there is less than a 1% chance (or, $\leq 2\%$ for SDSS J1631+2352) that the X-ray emission of each system is actually described by a single point source.
3. The posterior distributions returned by **BAYMAX** show that the best-fit locations of each multiple point source system coincide with the optical nuclei of galaxies within the merger (as determined by SDSS DR16) and all separations are inconsistent with 0 at the 99.7% C.L.
4. Running our spectral analysis on the multiple point source systems, we find that all point sources have unabsorbed 2 – 7 keV luminosities greater than 10^{40} erg s $^{-1}$, with the exception of the secondary point source in NGC 3341.
5. For the one system with a Bayes factors in favor of the single point source model, further investigation reflects that SDSS J0858+1822 likely hosts no AGN. Classifying X-ray point sources with $L_{2-7\text{keV}} > 10^{41}$ erg s $^{-1}$ as bona fida AGN, we conclude that NGC 3341 is a single AGN system, while SDSS J161+2352, SDSS J1708+2153, SDSS J2356–1016, and SDSS J0849+1114 have at least one AGN (the primary point source in all cases). A multi-wavelength analysis is required for a bet-

ter understanding of the true duality, or triality, of all these systems.

ACKNOWLEDGEMENTS

We thank our referee for thorough and thoughtful feedback, which strengthened our analysis and results. A.F. and K.G. acknowledge support provided by the National Aeronautics and Space Administration through Chandra Award Numbers TM8-19007X, GO7-18087X, and GO8-19078X, issued by the Chandra X-ray Observatory Center, which is operated by the Smithsonian Astrophysical Observatory for and on behalf of the National Aeronautics Space Administration under contract NAS8-03060. A.F. also acknowledges support provided by the National Aeronautics and Space Administration through Chandra proposal ID 21700319. MK acknowledges support from NASA through ADAP award 80NSSC19K0749. The scientific results reported in this article are based on data obtained from the *Chandra Data* Archive. This research has made use of NASA's Astrophysics Data System.

Software: CIAO (v4.8; [Fruscione et al. 2006](#)), XSPEC (v12.9.0; [Arnaud 1996](#)), *nestle* (<https://github.com/kbarbary/nestle>), PyMC3 ([Salvatier et al. 2016](#)), MARX (v5.3.3; [Davis et al. 2012](#))

REFERENCES

- Ahumada, R., Allende Prieto, C., Almeida, A., et al. 2019, arXiv e-prints, arXiv:1912.02905
- Anglés-Alcázar, D., Davé, R., Faucher-Giguère, C.-A., Özel, F., & Hopkins, P. F. 2017, MNRAS, 464, 2840
- Arnaud, K. A. 1996, in *Astronomical Society of the Pacific Conference Series*, Vol. 101, *Astronomical Data Analysis Software and Systems V*, ed. G. H. Jacoby & J. Barnes, 17
- Barnes, J. E., & Hernquist, L. E. 1991, ApJL, 370, L65
- Barth, A. J., Bentz, M. C., Greene, J. E., & Ho, L. C. 2008, ApJL, 683, L119
- Begelman, M. C., Blandford, R. D., & Rees, M. J. 1980, Nature, 287, 307
- Bianchi, S., Piconcelli, E., Pérez-Torres, M. Á., et al. 2013, MNRAS, 435, 2335
- Blaes, O., Lee, M. H., & Socrates, A. 2002, ApJ, 578, 775
- Blecha, L., Snyder, G. F., Satyapal, S., & Ellison, S. L. 2018, MNRAS, 478, 3056
- Brassington, N. J., Ponman, T. J., & Read, A. M. 2007, MNRAS, 377, 1439
- Brightman, M., & Nandra, K. 2011, MNRAS, 413, 1206
- Brightman, M., Nandra, K., Salvato, M., et al. 2014, MNRAS, 443, 1999
- Brightman, M., & Ueda, Y. 2012, MNRAS, 423, 702
- Cash, W. 1979, ApJ, 228, 939
- Comerford, J. M., Pooley, D., Barrows, R. S., et al. 2015, ApJ, 806, 219
- Corral, A., Della Ceca, R., Caccianiga, A., et al. 2011, A&A, 530, A42
- Cox, T. J., Di Matteo, T., Hernquist, L., et al. 2006, ApJ, 643, 692
- Csabai, I., Dobos, L., Trencsényi, M., et al. 2007, *Astronomische Nachrichten*, 328, 852
- Davis, J. E. 2001, ApJ, 562, 575
- Davis, J. E., Bautz, M. W., Dewey, D., et al. 2012, in *Proc. SPIE*, Vol. 8443, *Space Telescopes and Instrumentation 2012: Ultraviolet to Gamma Ray*, 84431A

- De Rosa, A., Bianchi, S., Bogdanović, T., et al. 2015, *Monthly Notices of the Royal Astronomical Society*, 453, 214. <https://doi.org/10.1093/mnras/stv1623>
- De Rosa, A., Vignali, C., Husemann, B., et al. 2018, *MNRAS*, 480, 1639
- De Rosa, A., Vignali, C., Bogdanović, T., et al. 2019, *NewAR*, 86, 101525
- Deane, R. P., Paragi, Z., Jarvis, M. J., et al. 2014, *Nature*, 511, 57
- Di Matteo, T., Colberg, J., Springel, V., Hernquist, L., & Sijacki, D. 2008, *ApJ*, 676, 33
- Duffell, P. C., D’Orazio, D., Derdzinski, A., et al. 2019, *arXiv*, arXiv:1911.05506
- Dvorkin, I., & Barausse, E. 2017, *MNRAS*, 470, 4547
- Foord, A., Gallo, E., Hodges-Kluck, E., et al. 2017a, *ApJ*, 841, 51
- Foord, A., Gültekin, K., Nevin, R., et al. 2020, *ApJ*, 892, 29
- Foord, A., Gültekin, K., Reynolds, M., et al. 2017b, *ApJ*, 851, 106
- Foord, A., Gültekin, K., Reynolds, M. T., et al. 2019, *ApJ*, 877, 17
- Fruscione, A., McDowell, J. C., Allen, G. E., et al. 2006, in *Society of Photo-Optical Instrumentation Engineers (SPIE) Conference Series*, Vol. 6270, Society of Photo-Optical Instrumentation Engineers (SPIE) Conference Series, 62701V
- Gehrels, N. 1986, *ApJ*, 303, 336
- Gross, A. C., Fu, H., Myers, A. D., Wrobel, J. M., & Djorgovski, S. G. 2019, *ApJ*, 883, 50
- Hopkins, P. F., Kereš, D., Murray, N., et al. 2013, *MNRAS*, 433, 78
- Hou, M., Li, Z., & Liu, X. 2020, *ApJ*, 900, 79
- Husemann, B., Heidt, J., De Rosa, A., et al. 2020, *A&A*, 639, A117
- Jeffreys, H. 1935, *Proceedings of the Cambridge Philosophical Society*, 31, 203
- Jeffreys, H. 1961, *Theory of probability*, Clarendon, Oxford
- Juda, M., & Karovska, M. 2010, in *Bulletin of the American Astronomical Society*, Vol. 42, AAS/High Energy Astrophysics Division #11, 722
- Kalberla, P. M. W., Burton, W. B., Hartmann, D., et al. 2005, *A&A*, 440, 775
- Kalfountzou, E., Santos Lleo, M., & Trichas, M. 2017, *ApJL*, 851, L15
- Kass, R. E., & Raftery, A. E. 1995, *Journal of the American Statistical Association*, 90, 773
- Kelley, L. Z., Blecha, L., & Hernquist, L. 2017, *MNRAS*, 464, 3131
- Kocevski, D. D., Brightman, M., Nandra, K., et al. 2015, *ApJ*, 814, 104
- Koss, M., Mushotzky, R., Treister, E., et al. 2012, *ApJL*, 746, L22
- Koss, M., Mushotzky, R., Veilleux, S., & Winter, L. 2010, *ApJL*, 716, L125
- Koss, M., Mushotzky, R., Treister, E., et al. 2011, *ApJL*, 735, L42
- Koss, M. J., Romero-Cañizales, C., Baronchelli, L., et al. 2015, *ApJ*, 807, 149
- Koss, M. J., Assef, R., Baloković, M., et al. 2016, *ApJ*, 825, 85
- Koss, M. J., Blecha, L., Bernhard, P., et al. 2018, *Nature*, 563, 214
- Lamastra, A., Bianchi, S., Matt, G., et al. 2009, *A&A*, 504, 73
- Lanzuisi, G., Civano, F., Marchesi, S., et al. 2018, *MNRAS*, 480, 2578
- Lehmer, B. D., Eufrazio, R. T., Tzanavaris, P., et al. 2019, *ApJS*, 243, 3
- Liu, X., Civano, F., Shen, Y., et al. 2013, *ApJ*, 762, 110
- Liu, X., Shen, Y., & Strauss, M. A. 2011a, *ApJL*, 736, L7
- Liu, X., Shen, Y., Strauss, M. A., & Hao, L. 2011b, *ApJ*, 737, 101
- Liu, X., Hou, M., Li, Z., et al. 2019, *ApJ*, 887, 90
- Marchesi, S., Ajello, M., Marcotulli, L., et al. 2018, *ApJ*, 854, 49
- Marinucci, A., Bianchi, S., Nicastro, F., Matt, G., & Goulding, A. D. 2012, *ApJ*, 748, 130
- Merritt, D., & Valluri, M. 1996, *ApJ*, 471, 82
- Milosavljević, M., & Merritt, D. 2003, *ApJ*, 596, 860
- Mineo, S., Gilfanov, M., & Sunyaev, R. 2012, *MNRAS*, 419, 2095
- Muñoz, D. J., Miranda, R., & Lai, D. 2019, *ApJ*, 871, 84
- Nevin, R., Comerford, J., Müller-Sánchez, F., Barrows, R., & Cooper, M. 2016, *ApJ*, 832, 67
- Panessa, F., Barcons, X., Bassani, L., et al. 2007, *A&A*, 467, 519
- Panessa, F., Bassani, L., Cappi, M., et al. 2006, *A&A*, 455, 173
- Perets, H. B., & Alexander, T. 2008, *ApJ*, 677, 146
- Pfeifle, R. W., Satyapal, S., Manzano-King, C., et al. 2019a, *ApJ*, 883, 167
- Pfeifle, R. W., Satyapal, S., Secrest, N. J., et al. 2019b, *ApJ*, 875, 117
- Ricci, C., Bauer, F. E., Treister, E., et al. 2017a, *MNRAS*, 468, 1273
- Ricci, C., Trakhtenbrot, B., Koss, M. J., et al. 2017b, *ApJS*, 233, 17
- Risaliti, G., Maiolino, R., & Salvati, M. 1999, *ApJ*, 522, 157
- Ryu, T., Perna, R., Haiman, Z., Ostriker, J. P., & Stone, N. C. 2018, *MNRAS*, 473, 3410

- Salvatier, J., Wiecki, T., & Fonnesbeck, C. 2016, *PeerJ Computer Science*, 2, 1507.08050
- Sazonov, S., & Khabibullin, I. 2017, *MNRAS*, 466, 1019
- Schawinski, K., Simmons, B. D., Urry, C. M., Treister, E., & Glikman, E. 2012, *MNRAS*, 425, L61
- Secrest, N. J., Dudik, R. P., Dorland, B. N., et al. 2015, *ApJS*, 221, 12
- Sinha, M., & Holley-Bockelmann, K. 2009, *MNRAS*, 397, 190
- Skilling, J. 2004, in *American Institute of Physics Conference Series*, Vol. 735, American Institute of Physics Conference Series, ed. R. Fischer, R. Preuss, & U. V. Toussaint, 395–405
- Smith, B. J., Campbell, K., Struck, C., et al. 2018, *AJ*, 155, 81
- Swartz, D. A., Soria, R., Tennant, A. F., & Yukita, M. 2011, *ApJ*, 741, 49
- Torres-Albà, N., Iwasawa, K., Díaz-Santos, T., et al. 2018, *A&A*, 620, A140
- Tozzi, P., Gilli, R., Mainieri, V., et al. 2006, *A&A*, 451, 457
- Tremmel, M., Governato, F., Volonteri, M., & Quinn, T. R. 2015, *MNRAS*, 451, 1868
- Vasiliev, E., Antonini, F., & Merritt, D. 2015, *ApJ*, 810, 49
- Walton, D. J., Roberts, T. P., Mateos, S., & Heard, V. 2011, *MNRAS*, 416, 1844
- White, S. D. M., & Rees, M. J. 1978, *MNRAS*, 183, 341
- Yan, C.-S., Lu, Y., Dai, X., & Yu, Q. 2015, *ApJ*, 809, 117